THESIS FOR THE DEGREE OF DOCTOR OF ENGINEERING

First Principles Calculations for NO_X Reduction over Ag/Al_2O_3

SIMON KLACAR

Department of Applied Physics
CHALMERS UNIVERSITY OF TECHNOLOGY
Göteborg, Sweden 2013

First Principles Calculations for NO_X Reduction over Ag/Al_2O_3
SIMON KLACAR
ISBN: 978-91-7385-863-2

Doktorsavhandlingar vid Chalmers tekniska högskola
Ny serie nr. 3544
ISSN: 0346-718X

Department of Applied Physics
Chalmers University of Technology
SE-412 96 Göteborg, Sweden
Telephone: +46 (0)31 772 1000

Printed by:
Chalmers Reproservice
Göteborg, Sweden 2013

First Principles Calculations for NO_X Reduction over Ag/Al_2O_3

Simon Klacar
Department of Applied Physics
Chalmers University of Technology, Göteborg 2013

Abstract

The importance of environmental awareness is today undisputed and manifests in tighter legislations for emissions of pollutants in stationary and automotive sources. This coincides with introduction of lean burn combustion engines in order to enhance the energy efficiency. These type of engines, however, pose a challenge due to inefficient reduction of nitrogen oxide species (NO_X) using the conventional three-way catalyst.

Selective catalytic reduction (SCR) with either ammonia (NH_3) or hydrocarbons (HC) as reducing agent offers a possible solution to the NO_X reduction issue. A promising candidate for NO_X reduction under HC-SCR and lean conditions, is silver supported on γ-alumina (Ag/Al_2O_3). However, despite much effort, many fundamental properties of the catalyst remain elusive. This includes the active phase, the role and charge state of Ag and the reaction mechanisms during reduction. Previous studies have suggested the presence of small Ag_n clusters, metallic, ionic, and oxidized silver phases. However, the importance and role of each phase is unclear. In order to understand and improve the catalyst, these issues, among others, need clarification.

Electronic structure calculations are performed in order to address the active site, the charge state of Ag, and to probe different reaction mechanism for lean NO_X reduction over Ag/Al_2O_3. Structural, energetic, electronic, and thermodynamic properties of Ag phases in different size and oxidation regimes are investigated and their reactivity towards O_2, NO_X, CO, and H_2 is evaluated. Based on NH_3 assisted SCR, reduction of NO_X is calculated to be facile over partially oxidized Ag and hydroxylated Al_2O_3 with intermediate formation of NH_2NO. Reduction over alumina requires the presence of NO and NO_2 wheras nitrites are suggested to limit the reduction over oxidized Ag.

The results are used to make general conclusions about lean NO_X-SCR over Ag/Al_2O_3.

Keywords: Ag, silver, oxygen, clusters, lean NO_X, reduction, alumina, catalyst, HC-SCR, NH_3-SCR, density functional theory, DFT, XPS, core level shifts

List of Publications

This thesis is based on the work presented in the following publications:

Paper 1 **High coverage oxygen induced surface structures on Ag(111)**
N. M. Martin, S. Klacar, H. Grönbeck, J. Knudsen, J. Schnadt, S. Blomberg, J. Gustafson, and E. Lundgren
In manuscript.

Paper 2 **Mechanism for reversed photoemission core-level shifts of oxidized Ag**
H. Grönbeck, S. Klacar, N. M. Martin, A. Hellman, E. Lundgren, and J. N. Andersen
Physical Review B, **85** (2012) 115445.

Paper 3 **Carbonate formation on $p(4\times4)$-O/Ag(111)**
J. Knudsen, N. M. Martin, E. Grånäs, S. Blomberg, J. Gustafson, J. N. Andersen, E. Lundgren, S. Klacar, A. Hellman, and H. Grönbeck
Physical Review B, **84** (2011) 115430.

Paper 4 **Facile NO_X interconversion over preoxidized Ag(111)**
S. Klacar, N. M. Martin, J. Gustafson, S. Blomberg, Z. Liu, S. Axnanda, R. Chang, E. Lundgren, and H. Grönbeck
Submitted to *Surface Science.*

Paper 5 **Oxidation of Small Silver Clusters: A Density Functional Theory Study**
S. Klacar, A. Hellman, I. Panas, and H. Grönbeck
Journal of Physical Chemistry C, **114** (2010) 268.

Paper 6 **H_2 dissociation over Ag/Al_2O_3: the first step in hydrogen assisted selective catalytic reduction of NO_X**
S. Klacar and H. Grönbeck
Catalysis Science & Technology, **3** (2013) 183.

Paper 7 **NO_X-SCR over Ag/Al_2O_3 from density functional theory calculations**
S. Klacar and H. Grönbeck
Submitted to *ACS Catalysis.*

Related publications not included in this thesis:

Low Temperature CO Oxidation over Supported Ultrathin MgO Films
A. Hellman, S. Klacar, and H. Grönbeck
Journal of the American Chemical Society, **131** (2009) 16636.

Phase Separation at the Nanoscale: Structural Properties of BaO Segregates on MgO-Based Nanoparticles
A. Sternig, S. Klacar, J. Bernardi, M. Stöger-Pollach, H. Grönbeck, and O. Diwald
Journal of Physical Chemistry C, **115** (2011) 15853.

How oxidized are small transition metal clusters?
A. Trinchero, L. O. Paz-Borbon, S. Klacar, A. Hellman, and H. Grönbeck
In manuscript.

My contributions to the publications

Paper 1
I performed all the calculations and took part in discussions with all the authors regarding the results and drafted part of the manuscript.

Paper 2
My contribution to this paper consisted of calculations for the reconstructed silver system and discussions of results and manuscript with the other authors.

Paper 3
I performed all calculations and wrote the first draft of the computational part of the paper.

Paper 4
I performed all the calculations, the initial analysis of the results, and wrote the first draft of the paper.

Paper 5
I performed all the calculations, the initial analysis of the results, and wrote the first draft of the paper.

Paper 6
I performed all the calculations, the initial analysis of the results, and wrote the first draft of the paper.

Paper 7
I performed all the calculations, the initial analysis of the results, and wrote the first draft of the paper.

Table of Contents

1 Introduction

Catalysis exists today as an almost silent technology that forms the basis of chemical industry and provides viable routes for sustainable energy systems and pollution control. The catalytic synthesis of ammonia is one example. It is an essential constituent in the production of inorganic fertilizers, and rated as one of the most important findings during the 20th century [1]. This particular catalytic process was discovered by Fritz Haber in 1908 and later adapted for industrial production by Carl Bosch, Alvin Mittasch and their coworkers at BASF (Badische Anilin- und Soda- Fabrik). The process is a product from a technological era primarily characterized by experimental trial- and error. It is said that the team, led by Bosch, performed more than 6500 experiments, considering over 2500 catalyst formulations in their research, finally leading to the accepted iron-based catalyst [2]. At the present, research within catalysis, and, in particular, heterogeneous catalysis has entered a phase marked with a vision of directed catalyst design. Thanks to the rapid development of surface science and vacuum technology during the 70's, novel possibilities to probe surface phenomena, and characterize matter with atomic resolution are at hand. Staying with the example of ammonia synthesis, the initial dissociation of N_2 is often considered as the rate determining step (RDS) of the reaction. Dahl *et al.* [3] have demonstrated that the dissociation reaction over a Ru(0001) surface is completely dominated by atomic steps, which is a consequence of the geometrical and electronic structure of surface edge atoms. The example shows how progress of experimental techniques give access to fundamental atomic scale knowledge and enables catalyst design. Another example of this approach is Haldor Topsoe's BRIM catalyst. Based on atom-resolved scanning tunneling microscopy (STM) images, hydrotreating reactions over MoS_2 nano-clusters could be assigned to specific sites on the edges of these structures [4]. As a consequence, it was possible to develop preparation techniques that led to catalysts with increased hydrogenative activity.

Today, experimental progress is often made together with atomistic calculations. In fact, in the studies by Dahl *et al.* [3] and Lauritsen *et al.* [4], it was the combination of experiments and theoretical first principles calculations lead to the fundamental understanding of the active sites. It could therefore be argued that it is the parallel advancements in experimental surface science and the the rapid development of electronic structure software and computer processors that have paved the way for directed catalyst design. Computational catalysis offers a unique possibility for atomistic characterization of active sites and reaction mechanisms. Consequently, with the combined effort, crucial steps can be understood and ultimately used to improve the selectivity

and activity of a catalyst.

However, the lack of clear connection between surface science experiments, often based on UHV (ultra high vacuum) measurements involving clean and conducting samples,[1] and the situations[2] present during common catalytic processes, creates the so called pressure and materials gaps. More recent efforts and development of experimental analysis tools, and setups, have allowed for *in situ* measurements that can address the pressure and, to some extent, the materials gap. Measurements using common techniques such as STM, TEM (transmission electron microscopy), XRD (x-ray diffraction), and XPS (x-ray photoemission spectroscopy) can now be performed under fairly high pressures (10^{-3} atm), which allows for studies of many systems that are relevant for heterogeneous catalysts. In fact, the active phase of Pd during methane (CH_4) oxidation was recently unravelled in a combined DFT and *in situ* XRD study [5].

Also from purely a theoretical point of view, recent progress has made it possible to target the pressure and materials gap. With multiscale modelling, there is an established route to combine theoretical methods to address questions that span over several time and length scales. In heterogeneous catalysis, quantum mechanical calculations, such as density functional theory (DFT), can be used to understand the electronic structure of atomic complexes and surface structures. Adsorption energies and reaction barriers can be coupled to properties at the mesoscopic level via *ab initio* thermodynamics, Monte Carlo methods, and, in particular, kinetic modelling. Finally, at the macroscale, continuum-based models can be applied to address, for example, transport phenomena and mechanical properties.

1.1 Background

Using first principles electronic structure calculations, based on DFT, this thesis aims to address a particular issue that is related to exhaust-gas after-treatment. The problem stems from the early 70's when the U.S. Environmental Protection Agency set forward the first legislation to reduce the toxic emissions of CO and hydrocarbons (HC) in the major urban areas of California [6]. Driven by next-coming legislations, improvements in engine control, gasoline composition, and materials developments eventually resulted in the introduction of the three-way catalyst (TWC) [7, 8]. Characterized by a simultaneous ability to convert HC and CO through oxidation, and NO_X by reduction, this catalyst formulation has become a milestone in catalytic emission control technology. In a TWC, however, high conversion is only possible in a balanced red-ox exhaust. This is ensured by stoichiometric air-to-fuel ratio of $\sim$14.7 in the engine combustion chamber. Higher fuel contents (rich conditions) are generally associated with a fuel

[1] Real catalyst often consist of inhomogeneous, porous, multiphase materials in order to increase surface area and consequently activity and selectivity.

[2] Catalytic processes often occur at high pressures and elevated temperature, *e.g.* 1 atm and 500 K.

penalty and unwanted emissions of CO and HC while a high oxygen content (lean combustion) shifts the reaction equilibrium in favor of CO and HC oxidation reactions, and the NO_X conversion falls off rapidly. Because of this, only limited NO_X reduction is possible under oxygen excess by use of the TWC technology. Nevertheless, as lean combustion offers an advantageous fuel economy, lower exhaust gas temperatures, and reduced CO_2 emissions (per driven km), particular interest has been devoted to diesel and lean-burn engines where the air-to-fuel ratio is as high as 20. In order to allow for energy efficient combustion and still meet the continuously harder emission regulations, new technologies are needed.

Today, two main technologies are used for NO_X reduction in oxygen excess, namely NO_X storage and reduction (NSR) and selective catalytic reduction (SCR). In the NSR process [8], the engine is run under cyclic lean/rich conditions, shifting the air-to-fuel ratio from high to low. Following lean operation ($\sim$1 min), where a NO_X storage material is used to trap the nitrogen oxide species, a short rich phase ($\sim$1-2 s) allows for reduction of NO_X to N_2. In SCR, small amounts of a reducing agent, ammonia (NH_3) or hydrocarbons (HC), are injected into the engine exhaust. Due to infrastructure and transportation difficulties, NH_3-SCR has mostly been implemented in stationary applications such as power-plants and industrial plants. For mobile applications, the caustic and hazardous ammonia is replaced by aqueous urea that, by high temperature hydrolysis, forms NH_3 and CO_2. Today, ammonia SCR is the most effective lean NO_X technique and implemented in modern trucks. HC assisted SCR however, provides an appealing solution from an economical and a practical stand point given that all the necessary components already are present on the vehicle. Further development is, however, needed in order to increase the NO_X conversion and durability of a suitable catalyst.

In the literature, several different catalyst materials have been considered for HC-SCR. This includes zeolite-based [9–11] and refractory oxides such as zirconia [12, 13]. However, catalyst formulation based on a γ-alumina support has received particular attention owing to the high thermal and mechanical stability and favorable chemical properties. Alumina oxide is present in many phases of which mainly three are considered in catalytic applications. This includes α-, γ-, and η-alumina. α-alumina is the thermodynamically stable phase. It is crystalline, has a high thermal stability, and a low surface. The γ- and η-phases are porous and not yet structurally determined. For HC-SCR, the γ-alumina support has shown particular promise. The oxide has an inherent activity that is promoted by addition of transition metals, Co [13, 14], Cu [13, 15], Pt [13, 16–18], Pd [13, 16], Ir [16], Ru [16], Rh [13, 16], Mn [13], Ni [13], and in particular Ag [8, 11, 19–51]. In the case of silver, presence of small silver clusters ($Ag_n^{\delta+}$) [25,29,38,39], metallic silver (Ag^0) [25,31,36], oxidized silver (O-Ag) [25,34], and silver aluminate phases [29,31] have all been suggested and linked to the NO_X reduction activity. The existence of small Ag clusters has been demonstrated by various types

of experiments. In Ref. [39], characterization of Ag/Al_2O_3 using UV-vis spectroscopy indicates the presence of small silver clusters (Ag_n, n<10) as the optical spectra shows agreement with that of a zeolite structure in which one can assume to have atomic Ag. Extended X-ray adsorption fine structure (EXAFS) measurements [38] further support this claim as the average Ag-Ag coordination number is found to be ∼2.4, indicating the presence of trimers, Ag_3, and/or tetramers, Ag_4. Although the catalytic activity of Ag/Al_2O_3 is believed to be best facilitated by presence of both large particles and small clusters, this issue remains unclear. In the literature, Ag clusters are suggested to promote selectivity towards NO_X reduction under lean conditions [52], whereas metallic silver is known to facilitate oxidation reactions [19, 25, 26, 29, 31]. The optimal loading for NO_X chemistry during HC-SCR is reported to be ∼2 wt.% Ag. However, the cause remains under debate as recent report [53], based on XPS and UV-vis measurements, indicates a similar Ag size distribution despite an alternating metal loading.

At this point it is clear that despite the immense effort, where many properties of the Ag/Al_2O_3 system have been clarified, several fundamental aspects remain elusive. Commercial implementation of this particular catalyst is conditional on further development, which includes increased activity, selectivity, and stability. The most urgent issue is the lack of consensus regarding the active phase, and the elementary reactions. Unfortunately, direct surface science measurements over a γ-alumina supported sample are still not realistic as the oxide is nonconducting and structurally ill-defined. Instead, available information originates from measurements based on traditional catalyst testing methods. For example, the coverage and the nature of hydroxyl groups on the Al_2O_3 surface has proven important for the acid-base properties where as many as seven OH-stretching bands are reported by IR [54, 55]. Moreover, proton and aluminum NMR spectra [56] have provided the average Al-OH surface coordination, as well as local coordination of Al atoms in alumina bulk and presence of vacancies. This collective information has been important not only for the experimental work but also the theoretical progress where coordination numbers, oxidation states, vibrational data provide a basis on which a structural, atomistic model can be constructed.

An additional aspect of the Ag/Al_2O_3 catalyst, initially observed by Satokawa and coworkers [28, 29], and later repeated in several experiments [33, 36, 38–40, 46–49] is that addition of H_2, in small amounts, further promotes NO_X conversion with hydrocarbons and shifts the activation to lower temperatures. The origin of the "H_2-effect" is unknown but similar results are observed for NH_3 assisted reduction over silver alumina where almost 90% conversion, already at 200 °C, can be achieved in the presence of hydrogen [50, 57–60]. In fact, several publications indicate that NH_3-SCR also is an intermediate reaction in HC-SCR [30, 61, 62]. As ammonia assisted SCR probably presents a reduced complexity in reductant-NO_X interactions, it provides possible route in which to address some of the issues related to HC-SCR.

Several extensive reviews are available on the subject of lean NO_X reduction [8, 11,

63, 64], covering the history, the problems, and advances throughout the decades.

1.2 Objectives

This thesis focus on two different but important aspects of the Ag/Al_2O_3 catalyst which are relevant in connection to NO_X-SCR catalysis. One part is based on joint experimental and theoretical work, where well-defined atomistic models of the silver component are considered in order to study specific SCR reactions, such as CO and NO_X oxidation, but also to identify thermodynamically stable structures in the presence of O_2. Using models with reduced complexity enables studies where a direct comparison at the atomic level can be made between theory and experiments. This provides a route to understand the elementary properties of Ag within the context of SCR catalysis.

The second part is based on theoretical investigations of more complex systems that cannot easily be studied experimentally with atomistic control. This includes *e.g.* the structure and stability of oxidized sub-nano sized Ag clusters, and possible sites for H_2 dissociation over Ag/Al_2O_3. Finally, the two aspects are combined in a study of the SCR process over Ag/Al_2O_3, using NH_3 as a reducing agent. Possible reaction pathways for NO and NO_2 reduction are presented and the importance of the different components, such as the alumina substrate and the Ag_n clusters are investigated.

2 Electronic Structure Calculations

The electronic structure reflects how the electrons of an atom, a molecule or a piece of bulk material are spatially and energetically distributed. Based on the concepts of quantum mechanics, density functional theory (DFT) [65, 66] provides a framework in which the electronic structure and, in particular, the total energy can be obtained. The theory can be used, for example, to determine stable geometries, calculate binding energies, mechanical, optical, magnetic, and electronic properties of atoms, molecules, and condensed matter. Thanks to the general formulation, a large variety of systems and problems can be addressed, leading to an expanding user community with background in physics, chemistry, biology, and materials science.

This section provides a short summary of the fundamental points of the density functional formalism. Detailed treatment of the DFT can be found in the literature [67–70]. Here, focus will be placed on a particular scheme for implementing the density functional theory: the Kohn-Sham approach [66] where special attention is placed on formulations using linear combinations of atomic orbitals (LCAO) or plane-waves (PWs). The plane-wave formulation is considered in combination with pseudopotentials (PPs).

2.1 The Many-Body Problem

To study and analyze the stationary properties of matter, we need to solve the time-independent Schrödinger equation:

$$H_{tot}\Psi_{tot}(\mathbf{R},\mathbf{r}) = E_{tot}\Psi_{tot}(\mathbf{R},\mathbf{r}), \tag{2.1}$$

where H_{tot} is the total Hamiltonian, Ψ_{tot} the total many-body wavefunction, and E_{tot} the total energy of the system. Eq. 2.1 is a second order, partial differential equation, here written in the eigenvalue form. The many-body wavefunctions, Ψ_{tot}, are eigenfunctions with the corresponding energy eigenvalue E_{tot}. The lowest energy eigenvalue is the ground-state energy of the system E_0. All energies higher than E_0 correspond to excited states. Knowledge of Ψ_{tot} implicates that all physical and chemical properties of the system are determined.

Realizing that the electronic and nuclear degrees of freedom can be separated, owing to the the much larger mass of the nucleus as compared to the electron (at least three orders of magnitude), the problem can be simplified. This separation leads to a

many-body wavefunction in a separable form:

$$\Psi_{tot}(\mathbf{R}, \mathbf{r}) = \Psi_e(R, \mathbf{r})\Lambda(\mathbf{R}). \tag{2.2}$$

The total wavefunction is separated in an electronic, $\Psi_e(R, \mathbf{r})$, and a nuclear part, $\Lambda(\mathbf{R})$. This separation is referred to as the Born-Oppenheimer approximation (BOA) [71]. The initial problem can in this way be simplified to the time-independent, non-relativistic (or simply electronic) Schrödinger equation[1]:

$$H_e\Psi_e(\mathbf{r}_i) = E_e\Psi_e(\mathbf{r}_i), \tag{2.3a}$$

where

$$H_e = T_e + V_{e-e} + V_{ext}, \tag{2.3b}$$

$$T_e = -\frac{1}{2}\sum_i \nabla_i^2, \tag{2.3c}$$

and

$$V_{e-e} = \frac{1}{2}\sum_{i\neq j}\frac{1}{|\mathbf{r_i} - \mathbf{r_j}|}, \tag{2.3d}$$

are the kinetic energy (T_e) and the classical electron-electron Coulomb potential. V_{ext} is an external, time-independent potential, experienced by the electrons due to *e.g.* nuclei in the system. Solving the electronic problem yields the potential that the nuclei move in. Consequently, in a system of N nuclei located at $\mathbf{R}_i$, the total ground-state energy, E_{tot} can be expressed as a function of nuclei coordinates E($\mathbf{R}_i$). This yields the potential energy surface (PES).

However, even within the BO-approximation, the task at hand remains a formidable many-body problem for systems with more than one electron. Here, the solution is based on one of two theoretical routes. Within the chemistry community one has pursued a solution based on approximations of the electronic many-body wavefunction. These approximations are often based on the Hartree-Fock approach [69,70,72–76]. The other route, often applied in the physics community originates from early attempts to solve the electronic problem based on the total electron density. Independent of each other, Thomas [77] and Fermi [78] simultaneously suggested that it is possible to utilize the electron density $n(\mathbf{r})$ as the basic variable rather than the many-body wavefunction. This resulted in the most rudimentary version of the density functional theory; the Tomas-Fermi model. In a system of N interacting electrons, instead of having to solve a 3N-dimensional problem, as would be the case in a wavefunction approach, the problem is reduced to only 3 dimensions.

[1]Here, atomic units are used: $\hbar = \mathrm{m}_e = \mathrm{e} = \frac{1}{4\pi\varepsilon_0} = 1$

2.2 The Density Functional Formalism

Solutions to the N electron system defined by Eqs. 2.3a-d can in principle be used to construct an electron density $n(\mathbf{r})$. This implies that the external potential determines $n(\mathbf{r})$. Two theorems, proved in 1964 by Hohenberg and Kohn [65] state that also the opposite is true, thus that the external potential is defined by the density. Formally, the total energy of a system is a unique functional of the electronic density (to an additive constant) and by knowing the ground-state density (n_0) the ground-state energy (E_0) is unambiguously known. In mathematical terms:

$$E[n] = \int d\mathbf{r} n(\mathbf{r}) v_{ext}(\mathbf{r}) + F[n], \tag{2.4a}$$

and

$$E_0[n_0] = \int d\mathbf{r} n_0(\mathbf{r}) v_{ext}(\mathbf{r}) + F[n_0], \tag{2.4b}$$

where

$$F[n] = T_e[n] + V_{e-e}[n]. \tag{2.4c}$$

$F[n]$ is a *universal* functional with no dependence on the external potential. It contains both the kinetic and the Coulomb energy of the system. The ground-state energy is, thus, obtained through a minimization problem:

$$E_0 = \min_{n \epsilon N} E[n]. \tag{2.5}$$

A possible route to formally calculate n_0 and E_0 within the DFT formalism was put forward by Kohn and Sham [66] (KS) in 1965. In the present, most DFT implementations use this approach. The idea was to construct an effective potential v_{eff} for a fictive system (a KS system) of non-interacting electrons, so as to obtain an electron density that is identical to that of the real interacting system. The suggestion was to express the universal functional $F[n]$ as:

$$F[n] = \tilde{T}_e[n(\mathbf{r})] + \frac{1}{2} \int d\mathbf{r} \frac{n(\mathbf{r})}{|\mathbf{r} - \mathbf{r}'|} + E_{xc}[n(\mathbf{r})]. \tag{2.6}$$

$\tilde{T}_e$ is the kinetic energy of the non-interacting system with a density $n(\mathbf{r})$. The second term, often referred to as the Hartree energy, contains the classical, direct Coulomb energy. The exchange-correlation (xc) energy, E_{xc}, collects the difference in kinetic energy between the true (interacting) and fictions (non-interacting) systems ($\tilde{T}_e$ - T_e) as well as the non-direct electron-electron interaction; exchange and correlation contribution. As the Coulomb term includes the density of all electrons in the system, each electron is interacting with itself. This is referred to as self-interaction. In a Hartree-Fock formu-

lation, self-interaction is canceled thanks to the exact treatment of exchange. In DFT, these contributions will cancel if the true form of the exchange-correlation potential is known. Unfortunately, the exact form, including all the many-body effects, is unknown. Consequently, a critical point within density functional theory is to adequately approximate the exchange-correlation potential, defined by:

$$V_{xc} = \frac{\delta E_{xc}}{\delta n(\mathbf{r})}. \tag{2.7}$$

One of the first approaches was suggested by Kohn and Sham [66] and goes under the name local density approximation (LDA):

$$E_{xc}^{LDA}[n] = \int d\mathbf{r} n(\mathbf{r}) \epsilon_{xc}[n(\mathbf{r})]. \tag{2.8}$$

The idea is to consider the inhomogeneous system as locally homogeneous. Consequently, the local terms are calculated via an integral over the exchange-correlation energy per electron (ϵ_{xc}). Many of the problems related to the LDA approximation are due to the asymptotic, exponential decay of the constructed density. In reality it should fall off in a Coulomb-like (1/r) manner. Improvements over LDA have been suggested [68], where the most commonly used approach is to include density gradients. The energy within the so called generalized gradient approximation (GGA) is defined as:

$$E_{xc}^{GGA}[n] = \int d\mathbf{r} f(n(\mathbf{r}), |\nabla n(\mathbf{r})|). \tag{2.9}$$

Several functionals according to the GGA idea are available, including Perdew-Wang-91 (PW91) [79], Perdew-Burke-Ernzerhof (PBE) [80], revised PBE [81], and RPBE [82]. Calculations performed for different molecules and extended system, within LDA and several forms of and GGA functionals, compared to experimental data, are presented in Ref. [82–84]. Throughout the work presented here, PBE [80] has been used. In general, the success of GGA functionals, as compared to LDA, is improved agreement with experimental chemisorption, binding, and atomic energies, and bond lengths and angles. However, there is a limiting accuracy of the GGAs. It is traced back to the the exchange term and an inadequate description of the non-local contribution and presence of self-interaction in the Hartree term. Improvements to the xc-energy can be made at different levels of theory and generally they increase the computational cost. Beyond the GGAs are the meta-GGAs that also take into consideration the kinetic energy density. At even higher levels, using hybrid functionals involves adding a portion of exact exchange from Hartree-Fock theory to the exchange and correlation energy calculated from *e.g.* GGA calculations. The most common hybrid functional within DFT are PBE0 [85] and B3LYP [86].

With a form for $F[n]$ (Eq. 2.6) it can be shown that the minimization problem

suggested by Hohenberg and Kohn (Eq. 2.4a), under the constraint that the total number of electrons is conserved, leads to a set of KS-equations that can be solved for the KS-orbitals:

$$\left[-\frac{1}{2}\nabla^2 + v_{eff}\right]\phi_i(\mathbf{r}) = \epsilon_i\phi_i(\mathbf{r}), \tag{2.10a}$$

where

$$v_{eff} = v_{ext} + v_{e-e} + v_{xc}. \tag{2.10b}$$

The density is given by:

$$n(\mathbf{r}) = \sum_{i=1}^{N} \phi_i^*(\mathbf{r})\phi_i(\mathbf{r}). \tag{2.11}$$

The energy eigenvalues ϵ_i have no obvious physical meaning, they are a consequence of the applied variational principle and appear as Lagrange multipliers. In similarity, the physical meaning of the KS-orbitals $[\phi_i(\mathbf{r})]$ is unclear. They are constructed to satisfy the KS-equation (2.10a) and provide the correct electron density (Eq. 2.11). Despite this, practical experience indicates that much information is present in ϵ_i and $\phi_i(\mathbf{r})$, and they can be used to draw qualitative conclusions. After all, the KS-orbitals. $\phi_i(\mathbf{r})$, are associated with the electron density, $n(\mathbf{r})$, and the sum of ϵ_i is a large part of the total energy.

To solve the one-electron KS-equations (2.10a) the Hartree- and the xc-potentials need to be evaluated. However, they are a subject of the electron density. The density, is given by the KS-orbitals which in turn are obtained by solving the KS-equations. To break the circle, an iterative approach is used where the initial density is constructed using a set of trial orbitals $\{\phi_i\}_j$. The KS-equations are thereby solved for a new set $\{\phi_i\}_{j+1}$. If the new set is consistent with the old set the solution is found and the ground-state density has been obtained. In practice, the iterations are performed by mixing of new and old densities until calculated orbitals do not change from one cycle to another. This is referred to as the *self-consistent field* (SCF) loop.

2.3 The LCAO Approach

In application of DFT, the choice of expansion functions for the KS-orbitals $[\phi(\mathbf{r})]$ is centered around two main formulations. In computational chemistry, it is most common to expand the $\phi(\mathbf{r})$ in terms of localized orbitals $\varphi(\mathbf{r})$. This approach is referred to as linear combination of atomic orbitals (LCAO) [87]:

$$\phi_j(\mathbf{r}) = \sum_i c_{ij}\varphi_i(\mathbf{r}), \tag{2.12}$$

where the basis functions $\varphi(\mathbf{r})$ are centered at the atomic nuclei and c_{ij} are the corresponding expansion coefficients. The idea is that the distribution of electrons within a molecule, to a large extend, is correlated with the positions of the individual atoms. Consequently, a natural starting point is to generate a local basis set that reproduces the atomic orbitals (AOs). The basis can then be exported to molecular and bulk phases. Most common basis functions are analytic, such as Gaussians [88], or Slater-type of orbitals [89], but also numerical representations are available [90]. In Papers 5, 6, and 7 we have used the LCAO implementation with a numerical basis set where each orbital corresponds to an atomic orbital. As the variational freedom increases with the number of basis functions, often a second set of orbitals is generated, resulting in a double numerical basis (dn). Moreover, in order to allow for polarization effects on an specific atom, the basis is often complemented with functions for the it's ions; a dnp basis. Such a basis is associated with a computational cost but is in general considered to be more accurate. A large advantage with a numerical basis is it's compact form; few basis functions are needed for a good description of the KS-orbitals. For example, CO can be accurately described by 12 basis functions within a dnp basis. However, a drawback it that there is no systematical way to improve the basis set.

2.4 The Plane-Wave Basis

The second major route to orbital expansion is by means of plane-waves (PWs). If the LCAO method was "chemical" in it's approach, the plane-wave method is certainly more "physics-based" and originates from calculations of extended bulk and surface systems. Using Bloch's theorem, the KS-orbitals can be expressed as a product of a cell-periodic and a wave-like part:

$$\phi_j(\mathbf{r}) = u_j(\mathbf{r})e^{i\mathbf{k}\cdot\mathbf{r}}. \tag{2.13}$$

The cell periodic contribution can be written as a sum using a basis set of plane-waves where the wave vectors are the reciprocal lattice vectors $\mathbf{G}$:

$$u_j(\mathbf{r}) = \sum_{\mathbf{G}} c_{j,\mathbf{G}} e^{i\mathbf{G}\cdot\mathbf{r}}. \tag{2.14}$$

The reciprocal vectors are defined such that $\mathbf{G}\cdot\mathbf{a} = 2\pi\mathrm{n}$, where $\mathbf{a}$ are the real space lattice vectors and n is an integer. This leads to the final expression of the KS orbitals where each electronic wavefunction is written as a sum of plane-waves:

$$\phi_j(\mathbf{r}) = \sum_{\mathbf{G}} c_{j,\mathbf{k}+\mathbf{G}} e^{i(\mathbf{k}+\mathbf{G})\cdot\mathbf{r}}. \tag{2.15}$$

The summation runs over all wave vectors ($\mathbf{G}$). In practice, the expansion coefficients, $c_{j,\mathbf{G}}$, will decrease with increasing $|\mathbf{k}+\mathbf{G}|$. This suggests that a reduced set of plane-wave expansion terms needs to be considered: $|\mathbf{k}+\mathbf{G}|^2 \leq 2E_{cut}$. This is fortunate, as it provides a very simple way of controlling the computational accuracy. By tuning the cut-off energy, the basis set size changes accordingly together with the accuracy. One additional advantage with plane-wave expansion is that the basis is not dependent on atomic positions, which makes this method highly suitable for molecular dynamics calculations [91]. However a large number of plane-waves are needed. For example, in order to describe CO, around 18 000 plane-waves are needed.

2.5 Pseudopotentials

Core states are not affected by changes in bonding, nor do they directly contribute to bonding properties. Their importance is instead correlated to screening of the nucleus charge, forming an effective potential for the valence states. It is from the interactions between the valence states that the physical and chemical properties of molecules and solids are derived. Because the core states are of limited interest for bonding properties they are separated from the valence and initially considered to be frozen (frozen core approximation). Subsequently, they are entirely removed and the interactions between the valance electrons and the core are replaced by a fictitious, weaker potential; a pseudopotential. This is fortunate, because the rapid oscillations of core and valence states in the core region are difficult to describe and, for example, a plane-waves basis would require an impossible basis-set size. As the core is replaced by a pseudopotential it leads to a highly reduced basis set. For this reason, a plane-wave basis is always used with pseudopotentials. However, pseudopotentials are also used with in LCAO calculations, in which case they are referred to as *effective core potentials*. As opposed to plane-waves, localized basis functions already exhibit the sharp features in the core region, but because all-electron calculations in many cases are not practical it is desirable to use pseudopotentials. Finally, as the core is removed and modeled via an effective potential, it presents a very intuitive way to include relativistic effects which are important for heavy atoms.

Potentials are constructed such as to model the effect of the nucleus and core on the states in the valence:

$$V^{PP}(\mathbf{r}) = v_L^{PP}(\mathbf{r}) + \sum_l v_{NL}^{PP}(\mathbf{r})\hat{P}_l, \tag{2.16}$$

where $v_L^{PP}(\mathbf{r})$ is the local part. Orthogonality between the valence and core states are accounted for via a non-local part. The projection operators ($\hat{P}_l$) is used to project

out the different angular components of the wave function. When constructing pseudopotentials several conditions need to be fulfilled. The integrated charge within a cut-off radius, r_c, should agree between the all-electron (AE) and pseudo-descriptions. This property is often referred to as *norm-conservation* and among other things insures correct scattering properties. Moreover, calculations performed with the pseudopotentials should provide the same KS-eigenvalues, ϵ_i. Finally, it is important to choose a proper pseudization radius that will not affect the valence region and consequently the bonding states. However, with a smaller radius, a larger basis is needed, *i.e.* more plane-waves (larger cut-off); a property referred to as *hardness*. The construction procedure is based on first solving the Schrödinger equation for the atom in question (in an all-electron formulation). This allows for a formal expression of the nodeless pseudo

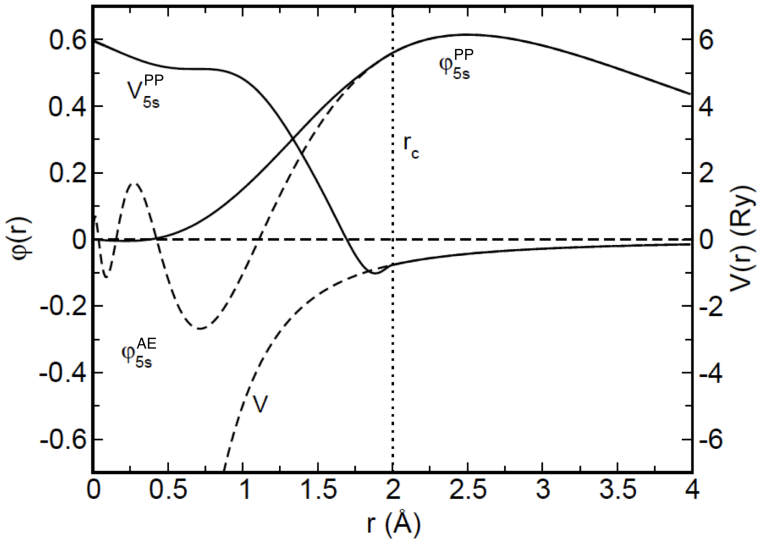

Figure 2.1: All electron (broken line) and pseudo wavefunction (solid line) for 5s electron of silver (Ag). The 5s pseudopotential is displayed (solid line) as well as the classical Coulomb potential (V) (broken line). r_c represents the cut-off radius.

wavefunctions that fulfill the mentioned requirements. The pseudopotential is finally obtained by inverting the Schrödinger equation. Hopefully the constructed pseudopotential has high *transferability*, meaning that the same potential can be transferred between different chemical environments and still produce accurate results. As the pseudopotentials are generated with a specific electronic configuration, the idea that the same potential could describe different configurations sometimes becomes questionable. For example, in an ionic material, such as MgO, the crystal contains Mg^{2+} and O^{2-} ions and not the neutral Mg and O atoms which often are used to construct the pseudopotentials. Thus, the chemical environment should be taken into account when generating the potentials.

Beyond the theoretical implementation, the most common potentials are norm-

conserving [92, 93] and ultrasoft [94]. Due to practical reasons, and often better transferability, ultrasoft pseudopotentials (UPPs), an plane-waves, were used in Papers 1-4. As the norm-conservation conditions are "softer" for UPPs, they require a smaller number of basis functions and thus smaller cut-off energies. This considerably affects the computational effort. The ultrasoft potentials, are, however, more difficult to construct.

Fig. 2.1 displays generated pseudopotentials [V_{5s}^{PP}] and wavefunctions [ϕ_{5s}^{PP}] for 5s electrons of silver (Ag). The all-electron (AE) counterparts (Coulomb potential (V), and wavefunction [ϕ_{5s}^{AE}] of Ag 5s), are also presented, displayed as broken lines. Within the cut-off radius (r_c) ϕ_{5s}^{AE} displays oscillatory variations, that would be difficult to handle within an AE description using plane-waves. The pseudo wavefunction, on the other hand is much smoother at $r < r_c$ and more attractive. The generated pseudopotential [V_{5s}^{PP}] is very different from the unscreened Coulomb potential (V) at $r < r_c$ as it is generated to emulate how the 5s electron experience their surrounding. Owing to classical and quantum effects they should consequently experience a repulsion when moving towards the core.

3 Modeling Materials Properties

Density functional theory is a first principles approach for electronic structure calculations. The theory is based on fundamental laws of physics and no fitting of parameters is used[1]. However, in order to perform DFT calculations, atomic structural models are necessary. In catalysis, this issue sometimes poses a true barrier as the materials often are ill-defined and sometimes even without proper long-range ordering, *e.g.* γ-alumina.

3.1 Cluster and Slab Approaches

Modeling all atoms in a large particle is not realistic. Consequently a strategy is needed to reduce the system size. At the present, most DFT calculations are centered around either a cluster- or a slab-approach where the choice is largely coupled to the basis set and the level at which exchange-correlation effects are included. A schematic representation of the two methods is shown in Fig. 3.1 in a top and side view. In order to further illustrate the idea, an adsorbate is added and shown as a black ring. Both methods can be used regardless of the atomic system at hand, and both can be implemented together with any method of solving the KS-eqs. 2.10a (most importantly the choice of basis set). The inclusion of periodic boundary conditions (PBC) is not restricted to one method or the other. Most commonly, however, the cluster models are associated with calculations in the gas-phase and do not involve periodic conditions. Molecules, clusters, and other gas-phase species are most suitably treated within this approach which was applied throughout Paper 5 when considering the structure of Ag_n clusters. The method can also be used for extended systems, such as surfaces, with the hope that only a limited number of atoms is needed to describe the local chemical and mechanical properties of a material. In that case, the cluster is often embedded in an array of point charges to simulate a crystalline environment and retain long-range electrostatics. This particular methodology has not been applied in any of the publications presented here.

For practical reasons the cluster approach is most often used in combination with local basis functions whereas the slab approach has no such preference. Most often the slab method is chosen in order to describe surfaces with periodic structure in the surface plane, see Fig. 3.1 (right). The broken lines represent the computational cell and can be taken as the crystal unit cell or integer repetitions of it, in which case it is

[1]Some xc-functionals within the density functional theory are, however, empirical in the sense that coefficients in the functional are fitted to reproduce experimental bond strengths and distances.

referred to as a supercell. The cell is repeated in the three spatial directions such as to imitate an infinite two dimensional surface.

The surface slab model is created by truncating the corresponding bulk mate-

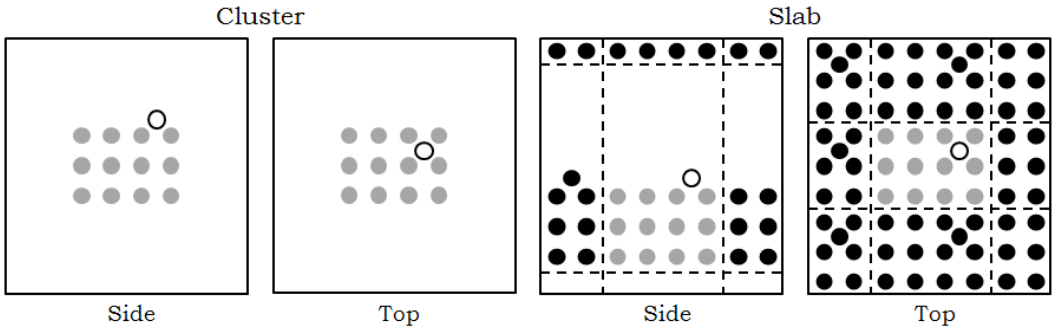

Figure 3.1: A schematic drawing, with top and side views, of a cluster and slab approach respectively. The cluster is composed of 46 atoms (12 atoms in each layer and three layers), whereas the slab approach displays a computational cell containing a slab with three atomic layers. Gray (rings) balls represent the substrate (adsorbate). The figure is inspired by [95].

rial in the desired crystallographic direction. However, in order to obtain a proper description of surface properties, also a correct description of the bulk material is vital. One main concern is related to electrostatic effects. For example, in oxides, the long-ranged Madelung contribution is of great importance for the electronic structure and consequently all properties derived from it. Truncating the bulk (in z-direction) leads to loss of long range ordering. To retain as much of these effects as possible, the slab thickness needs to be large enough, where often the bottom layers of the slab are kept fixed to their bulk positions in order to aid the description of the bulk material. Moreover, in a surface slab model, due to symmetry, one is always confronted with a slab containing two surfaces. Unless the number of atomic layers in the slab is large, unphysical interaction could take place between the two surfaces of the same slab. In general, the effects can take place whenever charged, or polar systems such as oxides and molecules, but also defects and steps are present. In any case, sufficient decay of the charge density can be ensured by placing a large enough vacuum width in all directions perpendicular to a surface or other truncation.

Similar electrostatic interactions can also propagate over the cell boundaries in the surface plane, *i.e.* xy direction. For example, modeling adsorption [Fig. 3.1 (right)] is always associated with coverage effects originating from electrostatics between adsorbates in neighboring computational cells. The effects of coverages can be modeled by considering the dilute case.

In any case, in a full modeling process, the atomic system is tested with respect to several modeling parameters where many of the electrostatic effects in the direction

of the surface normal are removed. This is illustrated in Fig. 3.2 where convergence with respect to differences in total energy (ΔE) per atom is [96, 97] considered as the vacuum size (top), number of atomic layers (middle), and k-point sampling (bottom) is changed. The calculations are performed for a metallic surface slab of Mg(0001) (left) and a metal-oxide MgO(100) surface (right). The results show that for a metallic Mg(0001), with a uniform charge distribution, an 8 Å vacuum distance and 5 atomic layers are sufficient to obtain convergence in energy differences, whereas the MgO(100) oxide surface (ionic) needs a substantially larger vacuum and should be modeled with a thicker slab, *e.g.* seven atomic layers.

Finally, total energy calculations involve evaluating integrals over the Brillouin

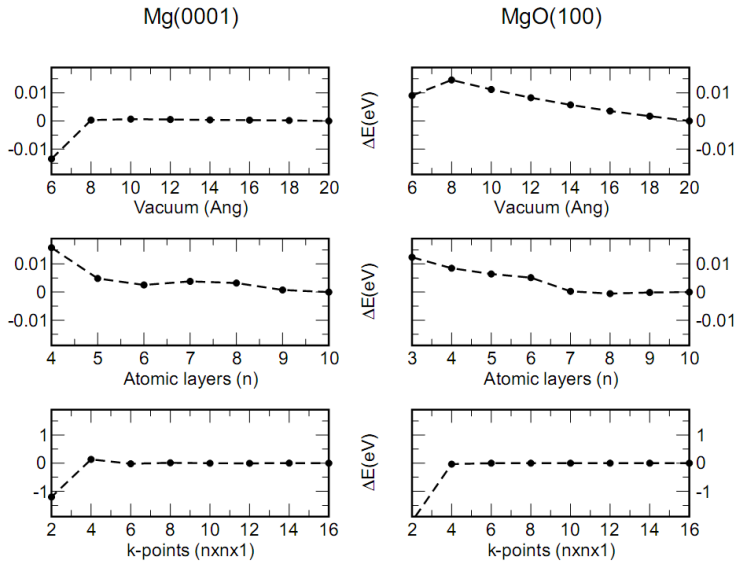

Figure 3.2: Convergence tests performed for a Mg(0001) surface (left) and MgO(100) surface (right). Energy convergence is considered for vacuum distance (top), number of atomic layers (middle), and k-point sampling (bottom). All energies are provided in eV and display the change (ΔE) in total energy per atom.

zone. Several approximations exist that allow us to consider a reduced set of k-points and replace the integration with a summation. The scheme suggested by Monkhorst and Pack [98, 99] is most widely used and has been applied throughout this work. In Fig. 3.1, bottom two panels, the k-point convergence test is displayed. The number of k-points used depends on the size of the computational cell but also on the material under scrutiny. Metals in general require a higher number of k-points owing to the dispersion relations that apply for electrons in metals. The large energy span over the y-axis in Fig. 3.1 (bottom) fails to correctly display the effects, but the metal does requires a larger set of k-points than the oxide in order to reach convergence.

3.2 Bridging DFT and Experiments

The density functional theory formalism allows to calculate the total energy and the corresponding ground-state density of an assembly of nuclei and electrons. Forces can later be evaluated and meta-stable structures can be obtained. With the structures and the electron density at hand, also other properties, besides the total energy, are available; many of which can be experimentally measured. This includes the structural information that can be correlated to measurements using imaging techniques *e.g.* diffraction (LEED) and microscopy (STM, TEM). Calculated adsorption energies and activation barriers can be experimentally determined with TPD and calorimetry. Measurements using spectroscopic methods such as IR and Raman spectroscopy, UPS, and XPS can be matched to calculated vibrational frequencies, density of states, and core-level binding energies, respectively.

3.2.1 The Potential Energy Surface

As mentioned, the solution of the electronic problem (KS-eq. 2.3a), yields the potential experienced by the nuclei. Comparing total energies of different geometrical structures as the nuclei are moved within that potential provides a possible route towards the lowest energy structure. However, more automatized and efficient procedures are present. In general, optimization is done by evaluating the forces ($\mathbf{F}$) acting on the ions:

$$\mathbf{F} = -\nabla_{\mathbf{R}_i} E. \tag{3.1}$$

The calculation is done according to the Hellmann-Feynman theorem [69, 70]:

$$\mathbf{F}(\mathbf{R}_i) = Z_i \sum_{ij} Z_j \frac{\mathbf{R}_i - \mathbf{R}_j}{|\mathbf{R}_i - \mathbf{R}_j|^3} + Z_i \int d\mathbf{r} n(\mathbf{r}) \frac{\mathbf{r} - \mathbf{R}_i}{|\mathbf{r} - \mathbf{R}_i|^3}, \tag{3.2}$$

and in a plane-wave description this is straightforward. However, as the force in an LCAO approach depends on the wavefunctions as well as the expansion of the basis set [100], Eq. 3.2 needs to be corrected with a term that depends on the basis. Minimizing the forces leads to a local minimum that could be the ground-state. However, often a local minimum, *i.e.* a metastable configuration, is reached. As there is no simple way to determine whether a minimum is the ground-state, some care is necessary. Probing the potential energy surface for small clusters ($n < 10$) is nowadays a rather facile process. By randomly generating hundreds, even thousands of geometrical shapes it is probable that ground-state is obtained. Still, as small clusters might have several closely lying electronic states, the issue of spin states needs special attention. This procedure was applied for all Ag_n structures in Paper 5. Unfortunately, this line

of action is not possible for larger systems due to high computational cost. In this case, atomistic modeling has to rely on experimental data where measured lattice distances, coordination numbers, and in the best of cases, visual data in form of STM images provides a basis for creating structure models.

3.2.2 Adsorption Energies

When an atom or molecule approaches a surface the combined system will rearrange so as to minimize the total energy. The adsorption energy is calculated by taking the differences in total energy between the two extremes, the non-interacting and final, relaxed systems. More formally, the adsorption energy E_{ads} for an adsorbate A is given by:

$$E_{ads}(A) = E_{A/S} - E_S - E_A, \tag{3.3}$$

where $E_{A/S}$, E_S, and E_A are the calculated total energies of the combined system (adsorbate and substrate), the bare substrate, and the adsorbate in the gas-phase. If the adsorption reaction is energetically favorable, the adsorption energy is negative; corresponding to the amount of energy required to pull the adsorbate (A) from the surface and put it into vacuum. To compare the stability of having a molecule in the gas-phase or dissociated on the surface, it is instead, convenient to use:

$$E_{ads}(A) = E_{A/S} - E_S - \frac{1}{2}E_{A_2}, \tag{3.4}$$

where E_{A_2} is the total energy of A_2. The values of the adsorption energies calculated with Eqs. 3.3 and 3.4 will differ owing to the the binding energy of the A_2 molecule.

3.2.3 Vibrational Frequencies

Vibrational frequencies are another good example of properties that can be obtained from electronic structure calculations. Using Eq. 3.2 and searching for stationary points on the PES, *i.e.* $\Delta\mathbf{F} = 0$, one can construct a second-derivative (mass-weighted) matrix of the energy, often referred to as the Hessian matrix [101]:

$$\mathbf{H}_{ij} = \frac{1}{\sqrt{m_i m_j}} \frac{\delta^2 E}{\delta q_i \delta q_j}. \tag{3.5}$$

Here, q_i and q_j refer to two coordinates of atoms i and j, with corresponding masses m_i and m_j. The second order derivatives are estimated with use of finite differences. Diagonalizing the Hessian matrix yields the corresponding eigenvalues (ϵ_k) and eigenvectors, which are the vibrational frequencies, $\epsilon_k = \omega_k^2$, and normal mode eigenvectors.

The frequencies are often calculated in the basis of the harmonic approximation where the limit of small atomic displacements is assumed. In classical mechanics, the equilibrium solution is defined by the potential energy of the system. However, in a quantum mechanical description,[2] the ground state solution for a harmonic oscillator has a kinetic contribution of size $h\omega/2$ (h is Planck's constant and ω is the calculated normal mode) and referred to as *zero-point energy*. Calculated adsorption energies via Eqs. 3.3 and 3.4 do not consider the zero-point contribution and are often corrected.

3.2.4 Activation Barriers

Density functional theory is routinely used to calculate transition barriers of chemical reactions. Beyond the mathematical and numerical implementation the ultimate goal is to find the energetically lowest first-order saddle point, along a path on the potential energy surface that connects a reactant and a product structure. This means that we are looking for a point on the PES at which the curvature, in all directions besides one, is positive. The idea is illustrated in a schematic representation of a potential energy surface in Fig. 3.3. The reactant structure, for example molecular adsorption of O_2 on Ag(111), is a local minima on the PES. In order to dissociate and reach the product, there is an activation barrier that needs to be climbed. We are looking for a path that renders the lowest possible barrier. The point along that path at which the first derivative of the energy changes and becomes negative is the transition state (TS) energy. Several methodologies have been developed to find transition states [102, 103]. All the transition barrier presented in this thesis, are estimated by a linear synchronous transit and quadratic synchronous transit method (LST/QST) [104]. Using linear interpolation, one can estimated the shortest possible path along the PES. This produces the LST path at which the energy maximum is a first guess of the TS state. In conjunction with a QST, that uses the same methodology but interpolates using three points, the LST-maximum is used during the QST-procedure as the intermediate structure for finer optimization and consecutive gradient minimization using conjugate gradient [105] method. So, by means of derivatives, interpolation and minimization procedures it is possible to estimate the transition state structure and the reaction path (QST path). To validate the TS, one can perform a frequency analysis on the TS-structure. If indeed it is the true energy maximum between the reactant and product the vibrational frequency calculation should yield at least one imaginary frequency. The other frequencies should be positive as a consequence of the gradient requirement. On a PES maximum (minimum), local or global, all frequencies are imaginary (real).

[2] In the classical case, the position and the momentum are both specified exactly. This is forbidden by Heisenbergs uncertainty principle in the case quantum mechanics.

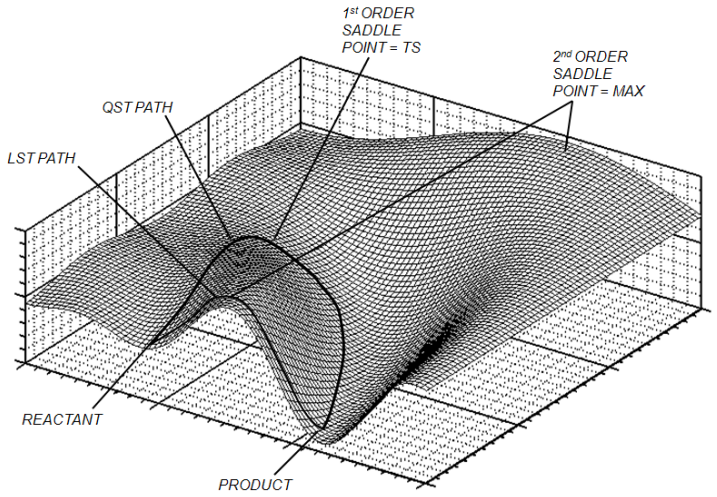

Figure 3.3: A schematic representation of a potential energy surface (PES). The REACTANT and PRODUCT energies are presented as local and absolute minima respectively. Transition barrier paths according to the LST and QST methods are presented along with stationary points that have been pointed out in order to aid further discussion.

3.2.5 *Ab initio* Thermodynamics

In our strive to use DFT results to predict properties at environmental conditions, the data obtained at zero Kelvin has to be coupled to the theory of thermodynamics. This is done within *ab initio* thermodynamics [106, 107]. It is based on the fact that in thermodynamical equilibrium with surrounding reference phases i, a system adopts the lowest free energy. It can do so by changing the number of atoms (n_i) of a particular reference phase as long as the minimization criterion is fulfilled. In a two-component systems, containing a surface slab under reaction conditions, pressure p and temperature T, and surrounding reference systems, *i.e.* bulk material and adsorbate, the surface free energy can be expressed as:

$$\gamma(p,T) = [G_{slab} - \sum_i n_i \mu_i(p,T)]/A, \tag{3.6}$$

where G_{slab} is the Gibbs free energy of the slab and A is the area of the computational cell. Moreover, the surface slab is in thermodynamical equilibrium with the surrounding atmosphere as well as the bulk material. This suggest that the chemical potentials $[\mu_i(T,p)]$ need to be included. As $\mu_i(T,p)$ depends on external conditions, temperature and pressure effects are included. The method was employed in Papers 1 an 5 to evaluate the thermodynamical stability of oxidized silver systems (clusters, surfaces and bulk oxide). In order to estimate the chemical potential of oxygen, the first approximation is to assume an ideal gas. The temperature dependence at p_0 (atmospheric

pressure) leads to:

$$\mu_{O_2}(T,p) = \mu_{O_2}(T,p_0) + k_B T ln(p/p_0), \tag{3.7}$$

expressed in terms of DFT energy, adding entropy (S) and enthalpy (H) effects:

$$\mu_{O_2}(T,p) = E_{O_2} + \Delta H - T\Delta S + k_B T ln(p/p_0), \tag{3.8a}$$

where

$$\Delta H = H(T,p_0) - H(0,p_0), \tag{3.8b}$$

and

$$\Delta S = S(T,p_0) - S(0,p_0), \tag{3.8c}$$

are taken from thermodynamical tables [108]. With this approach, all the translational, rotational and vibrational effects owing to temperature are included. This provides a way to investigate effects of temperatures and pressures, but also how the surface composition depends on these properties. The internal energies (enthalpies) are the calculated total energies in DFT calculations. Thus the Gibbs free energy of the slab, G_{slab}, can be written as:

$$G_{slab} = E_{slab} - E_{surf}, \tag{3.9}$$

where the calculated total energies of the slab, E_{slab}, and the clean substrate surface, E_{surf} are used. This approximation is valid for crystal phases, mainly because the differences in internal energy between different structures is larger than the entropic difference.

3.2.6 The Electronic Structure

One way to investigate the character of the bonds in the systems is to analyze the electronic density of states (DOS). As every element in the periodic table possess a unique electronic configuration, so do all material compositions. A hypothetical DOS is presented in Fig. 3.4 where also the corresponding energy states (E_n) are shown. A direct projection of the state-density on the energy provides the number of states per energy E, normalized to the total number N:

$$DOS = D(E) = \frac{1}{N}\sum_n \langle\phi_n|\phi_n\rangle\delta(E - E_n). \tag{3.10}$$

ϕ_n are the KS eigenstates. This representation allows for quick visualization of the electronic structure. Further information can be obtained by calculating the local or projected (LDOS/PDOS) density of states. Here, the nature of electron hybridization as well as correlation to experimental spectroscopic data can be derived. The

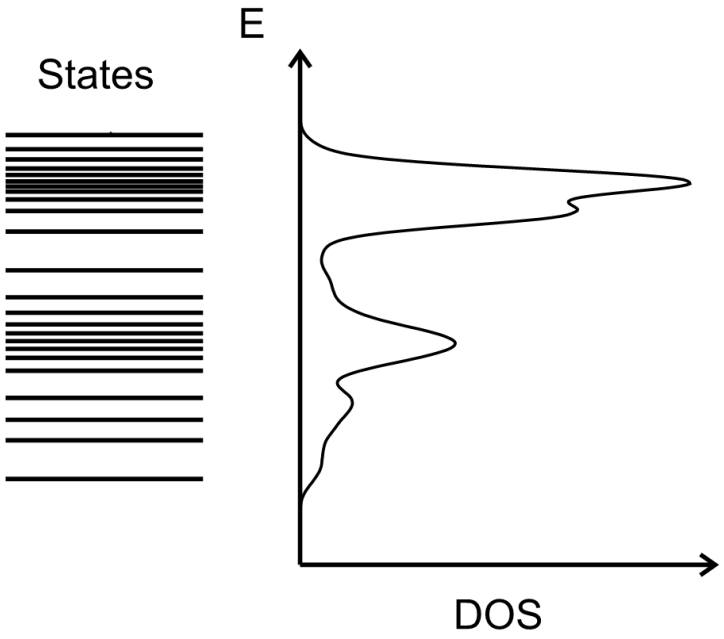

Figure 3.4: A schematic representation of a number of available states within an energy interval and the corresponding density of states (DOS).

LDOS demonstrates contribution of states derived from specific atoms in the system, to various regions of the energy spectrum:

$$LDOS = D(r, E) = \frac{1}{N} \sum_n \langle \phi_n | r \rangle \langle r | \phi_n \rangle \delta(E - E_n), \tag{3.11}$$

where the orbital projection (PDOS) can provide further resolution by considering contributions from different angular momenta:

$$PDOS = D_{lm}(E) = \frac{1}{N} \sum_n \langle \phi_n | \psi_{lm} \rangle \langle \psi_{lm} | \phi_n \rangle \delta(E - E_n). \tag{3.12}$$

Geometry and electronic structure optimization as well as interpretation of the electronic structure are very important as they aid the understanding of materials properties, help to clarify experimental results and, in the best of cases, predict new and stable structures. In this thesis, the access to the DOS (including the projected and local contributions) has been helpful on several occasions. This includes evaluation of Ag-O interaction in Papers 1, 2, and 5, and understanding H_2 dissociation in Paper 6. Moreover, it was via a combination of experimental measurements and DFT calculations that the surface structure of oxidized Ag(111) could be solved [109, 110]. By means of total energy comparison and supporting calculations of core level excitations

(addressed later), a final structure, called $p(4\times4)$-O/Ag(111), could be proposed. A similar methodology was used in Papers 3 and 5 in order to propose surface reconstructions of Ag(111) with one monolayer of carbonates/nitrates.

3.2.7 Scanning Tunneling Microscopy

The STM instrument was developed at IBM (Zürich) in 1981 by Gerd Binnig and Heinrich Rohrer for which they received the Nobel Price in Physics (1986) [111]. In short, a conducting metal tip is brought sufficiently close to the sample surface (<1 nm) to generate a finite probability for quantum mechanical tunneling. As a small voltage is applied over the junction, it results in a measurable current between the tip and the sample. Considering that the tunneling probability is exponentially dependent of the tip-sample distance, it is possible to scan the surface with the tip, and obtain a surface topology of the sample.

The quantitative theory of STM and in particular the tunneling current is often discussed on the basis of Bardeen's model [112]. He initially assumed that the solution to the Schrödinger equation is known for the two separate systems, the sample (S) and the tip (T) and, using time dependent perturbation theory, it can be shown that the probability of an electron to tunnel between sample state ψ_S, at E_S, and the tip state ψ_T, at E_S, is given by Fermi's golden rule:[3]

$$w = 2\pi|M|^2\delta(E_S - E_T), \tag{3.13}$$

where M is the tunneling matrix, calculated via a surface integral:

$$M = \frac{1}{2}\int d\vec{S}\cdot(\psi_T^*\vec{\nabla}\psi_S - \psi_S^*\vec{\nabla}\psi_T). \tag{3.14}$$

at a surface within the vacuum (Fig. 3.5). By modelling the tip as a piece of Sommerfeld metal, where the electronic wavefunctions of the tip are assumed to be spherically symmetric functions, *i.e.* s-type functions (Fig. 3.5), Tersoff and Hamann [113] were able to apply Bardeen's results to STM. Under low applied bias this assumption leads to a tunneling current, that at the tip apex has the form of:

$$I(\mathbf{R}, V) \propto \int_{E_F-|eV|}^{E_F} dE'|\psi_S(\mathbf{R}, E')|^2. \tag{3.15}$$

The position of the tip is given by $\mathbf{R}$, and $\psi_S(\mathbf{R}, E')$ denotes the sample state function at some given energy E'. Lastly, E_F refers to the Fermi level of the sample and V is the applied voltage. Eq. 3.15 suggests that the signal of the simulated current is directly

[3]In atomic units.

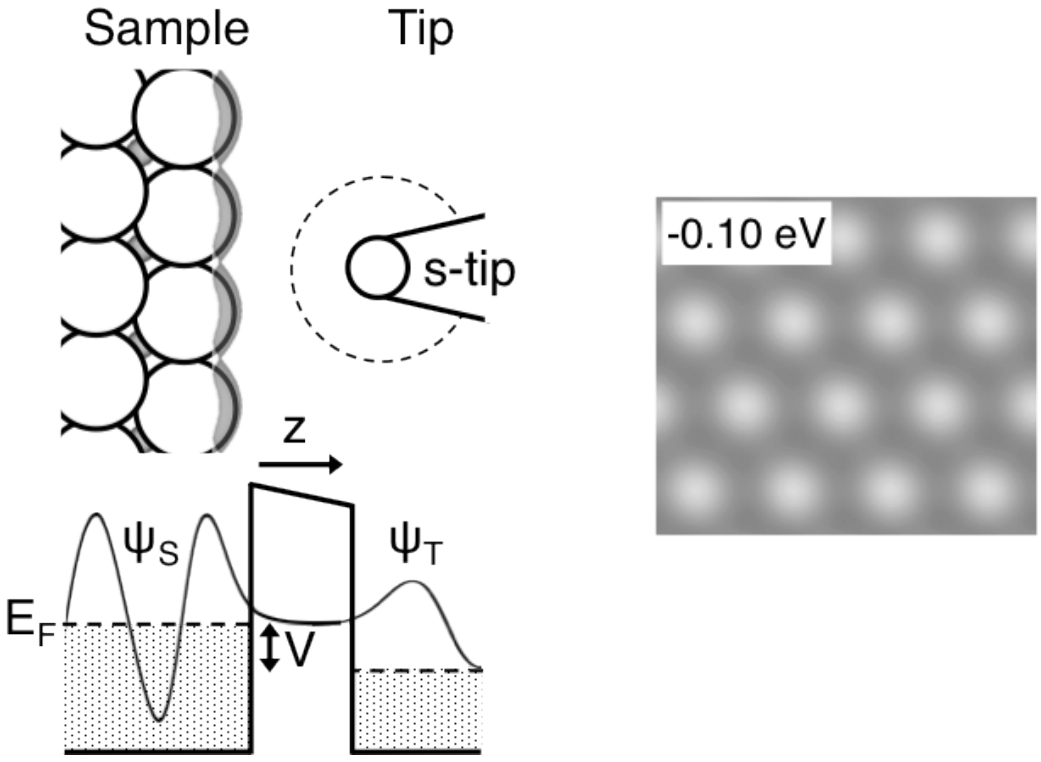

Figure 3.5: Bottom left: a schematic energy diagram of Bardeen's model with the sample (ψ_S) and tip states (ψ_T) separated by a potential barrier. Also, here, a (negative) voltage is applied (V), thus showing a situation where the occupied sample states are probed. z is the physical separation between the tip and sample. Top right: a two dimensional image of the Ag(111) surface where one constant density surface is shown (transparent grey). Right: simulated STM of Ag(111) with a negative bias of -0.10 eV and a constant height of 2.5 Å. The bright features represent the Ag surface atoms in a fcc lattice.

proportional to the local density of states at $\mathbf{R}$. Here, the integration is considered over occupied sample states $E \in [E_F - |eV|, E_F]$ with a negative applied bias (positive tip). A schematic representation of the situation is presented in Fig. 3.5 (left). In particular, in the left top panel, a schematic representation of the tip is shown along with a simulated Ag(111) surface with one isosurface of the density. During simulations, the LDOS is probed with the tip apex a distance $\mathbf{R}$ from the sample surface. The image in Fig. 3.5 (right) is a simulated STM spectra of the Ag(111) surface with V = -0.10 V, taken at a distance 2.5 Å from the surface. If the bias is positive (negative tip) one is instead probing the unoccupied states of the sample.

Simulating STM, in combination with DFT calculations is today possible in many first principle codes and provides in most cases reliable and good guidance of the sample structure, as shown in Fig. 3.5 (right). However, despite the agreement with experi-

mental STM spectra Ag(111) [114,115] the formula by Tersoff and Hamann has severe limitations that need to be considered. The model assumes low bias and consequently simulations need to be restructured to *e.g.* $< |\pm 0.10|$ V. Because of this, the method is not suitable for semiconductor. Moreover, a long lasting debate is the symmetry of the tip state. In the Tersoff-Hamann approach, the detailed structure of the tip wavefunctions is not included. Experimental STM tips, however, are often composed of tungsten (W) or an Pt/Ir alloy where d-derived states are present near the Fermi level. It has been suggested that the simulated tip states should have the symmetry of elongated d-like states [116, 117]. The subject is, however, under extensive research and several methods are being developed to accurately capture the interactions between the tip and the sample [118,119] including the possibility to explicitly model the tip structure [120].

3.2.8 Photoemission Core Level Shifts

Photoemission spectroscopy is an excellent experimental method for studying the geometry and the electronic structure of atoms, molecules, and surfaces. The shifts in core level signatures can also be calculated using first principle methods. In this thesis a PW-PP approach has been used. In order to calculate the shifts, pseudopotentials are generated based on the desired electronic configuration. In the case of Ag 3d (Papers 1-4) a pseudopotential with a $3d^9$ configuration is generated. Silver will be used throughout this section as an example where ultrasoft potentials are utilized. Shifts in core level binding energies of Ag surface atoms are calculated with respect to a reference state, often an atom deep in the bulk. The shift is given by:

$$\Delta_{cls} = E_{bulk} - E_{surf}, \tag{3.16}$$

where E_{surf} and E_{surf} are the total energies of two separate calculations with a core hole in a bulk and surface atom, respectively.

When generating pseudopotentials with an altered electronic configuration in the core we can choose i) a neutral or ii) an ionic potential. The two possibilities are presented in Fig. 3.6 for the Ag 5s electrons and denoted V^n_{5s} and V^i_{5s}, respectively. They are generated with a $3d^9$ configuration in the core. In the valence, however, V^n_{5s} is taken to be $4d^{10}5s^2$ whereas the ionic V^i_{5s} potential is $4d^{10}5s^1$. In order to discuss the difference, Fig. 3.6 is complemented with the regular Ag 5s potential (V_{5s}), with a $3d^{10}$ core and a $4d^{10}5s^1$ valence configuration.

Removing a Ag 3d core electron results in increased Coulomb attraction of valence states to the nucleus. The question then is how to best describe this state. With a $3d^9$ configuration in the core, a $4d^{10}5s^2$ valence is perhaps most appropriate as it reproduces the electronic relaxations and consequently the final state of the atom. For that reason, the V^n_{5s} pseudopotential largely overlaps with V_{5s} beyond the pseudization radius (r

$> r_c$). The ionic potential, V^i_{5s}, does, however, not explicitly account for decreased screening of the nucleus. This motivates the deviation from the V_{5s} potential in Fig. 3.6. Comparing the performance of the two potentials, the calculated core-level shifts for surface Ag(111) atoms (with respect to the bulk) are, however, similar with the two core-excited pseudopotentials. They are -0.17 and -0.19 eV using V^n_{5s} and V^i_{5s}, respectively. Moreover, V^n_{5s} and V^i_{5s} are found with the similar scattering properties and energy spectra. This suggests that the potentials have good transferability. In Papers 1-4, an ionic pseudopotential, with an $4d^{10}5s^1$ valence configuration is used.

Generating a pseudopotential with a desired core configuration and a suitable

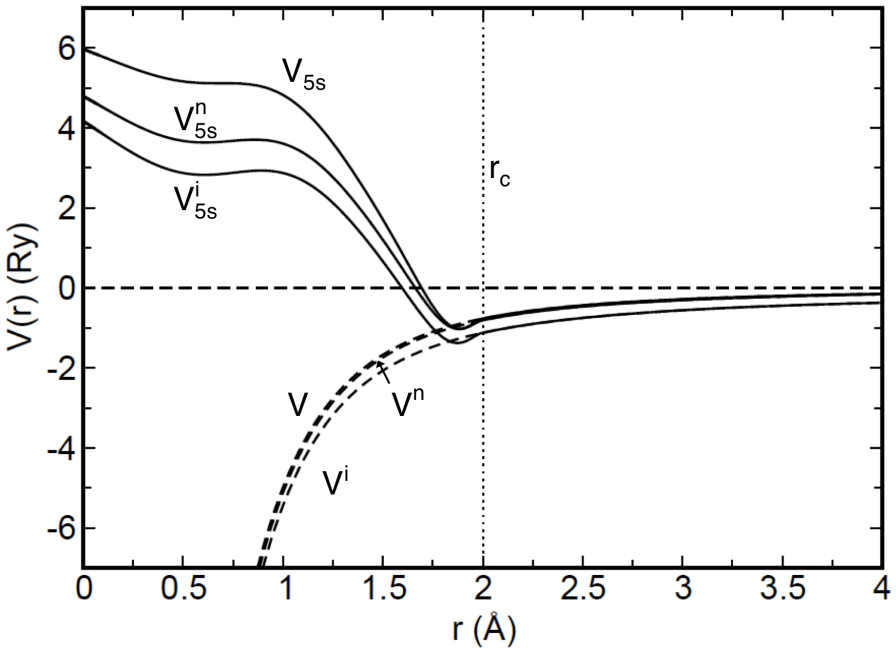

Figure 3.6: Generated pseudopotentials with an Ag $3d^{10}$ configuration (V_{5s}), and two PPs generated with a core hole in the Ag 3d: the neutral (V^n_{5s}) and the ionic (V^i_{5s}) pseudopotentials are shown. Also the corresponding Coulomb potentials are shown (broken lines). r_c represents the cut-off radius.

description of the final state is a very important step in order to calculate core level shifts. However, the generated potential can only account for the local changes in the electronic structure as a core electron is excited. There are also global effects that originate from the changes in the net charge of the system. The two approaches to address this issue are often referred to as i) neutral and ii) ionic ones. However, it should be noted that neither these approaches nor the global charge effects that they address are coupled to the choice of pseudopotential. In the neutral approach, the system, with a core hole, is calculated as formally anionic. This means that states above the Fermi energy will be populated during the calculations. In a metal, where there is no band-gap at the Fermi level, this can easily be accommodated via electronic

relaxation. In a semiconductor, or insulator, however, this approach could lead to new and unphysical properties, as one is occupying states in the conduction band. Consequently, the method is best suited for calculations of core level binding energies involving metallic systems. In the ionic approach a uniform electron gas, a jellium, is added to the computational cell in order to compensate for the net charge. This method is more general and can be applied to metals and oxides because the jellium does populate any electronic states. However, the uniform electron does interacts with the surface slab via the electrostatic potential. Consequently, it can be difficult to fully converge the calculated core level shifts with respect to the cell size, but also when comparing surfaces with different surface structures due to defects, vacancies, reconstructions, and adsorbates. However, as the effect of the jellium often are small, the work in this thesis is based on the ionic approach.

4 NO_X Reduction over Ag/Al_2O_3

Despite an extensive literature concerning NO_X catalysis over Ag/Al_2O_3 there is still a clear lack of consensus regarding several fundamental issues. Unfortunately, the issues are closely intertwined. There is uncertainty regarding i) the active phase, ii) the role of Ag, iii) the elementary steps, and iv) how H_2 promotes the reaction. These are issues that slow down the catalyst development.

This thesis contains a theoretical approach to NO_X reduction over Ag/Al_2O_3 and the mentioned issues. In Fig. 4.1, a schematic representation of the silver alumina catalyst is presented, based on the existing experimental and theoretical suggestions. It should be mentioned that an unambiguous structural characterization of the catalyst components is hindered by the ill-defined structure of γ-alumina. Evidence of small silver clusters (Ag_n) [25, 29, 38, 39], metallic silver (Ag^0) [25, 31, 36], oxidized silver (Ag-O) [25,34], and even silver aluminate phases [29,31] has been found. However, the importance of these phases has not been established. Unfortunately, neither has

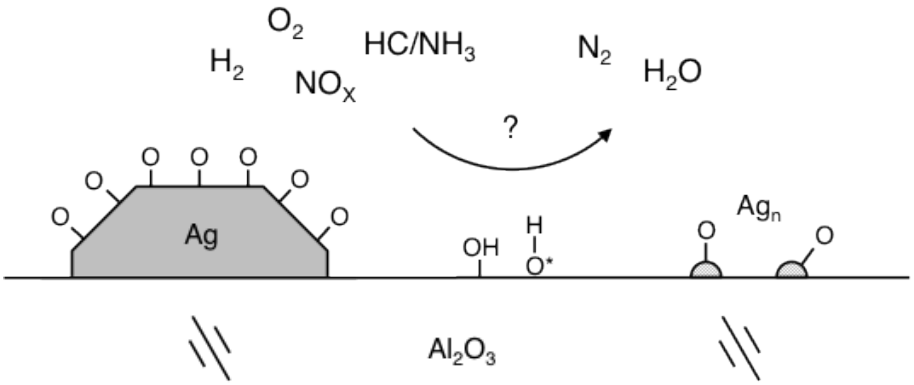

Figure 4.1: A schematic representation of the Ag/Al_2O_3 catalyst.

the role of the support (γ-alumina) which is known to be active towards NO_X reduction [50]. In the presence of water, Al_2O_3 is known to be hydroxylated [55] (Fig. 4.1). Using traditional experimental methods, *e.g* IR [54,121], XRD [55], temperature-programmed desorption (TPD) [122], electron energy loss spectroscopy (EELS) [123], and NMR [56,124], electronic and structural properties of γ-alumina has been investigated. For example, the coverage and average Al-OH coordination of hydroxyl groups on the Al_2O_3 surface has been probed and suggested [54, 55]. Moreover, beyond the catalyst structure and the active phase, the reaction mechanisms of NO_X-SCR have

received much attention (see Refs. [11, 41] for review). The experimental characterization is often based on *in situ* techniques, especially FTIR (fourier transform infrared) spectroscopy with focus on adsorbed NO_X species and intermediates during reduction. However, at this point, there are no generally accepted mechanisms. There are several HC-SCR reaction schemes proposed in the literature [11, 43, 125] where, the intermediate formation of amines and ammonia along the reduction path is accepted. This suggests that NH_3-SCR is part of HC-SCR. In the case of ammonia assisted SCR several experimental [126–132] and theoretical [133–140] studies have been able to establish the main NO_X reduction reactions. These are generally discussed on the basis of different NO:NO_2 ratios, namely standard- (1:0), fast- (1:1), and NO_2-SCR (0:1):

$$2NH_3 + 2NO + {}^1\!/_2O_2 \rightarrow 2N_2 + 3H_2O \qquad (standard - SCR) \tag{4.1a}$$

$$2NH_3 + NO + NO_2 \rightarrow 2N_2 + 3H_2O \qquad (fast - SCR) \tag{4.1b}$$

$$4NH_3 + 2NO_2 + O_2 \rightarrow 3N_2 + 6H_2O \qquad (NO_2 - SCR) \tag{4.1c}$$

The standard-SCR route (Eq. 4.1a) is often considered to be dominant as most of the exhaust from diesel and lean burn engines is composed of NO. The reaction is, however, associated with high temperatures [128]. Instead, much attention attention has been devoted to a fast-SCR scheme that where, for example, 80% NO_X conversion can be achieved at 225°C over a V-based catalyst [128]. NH_3-SCR is also considered over Ag/Al_2O_3 with even higher conversion (almost 90%) at temperatures as low as 200°C. However, reduction is only observed in the presence H_2. [50,57–60]. Despite the general reactions in Eq. 4.1, the detailed understanding of NH_3 reduction mechanisms is lacking, including knowledge of NH_3 and NO_X adsorption sites and intermediates.

4.1 State and Role of Ag

With the uncertainties, a natural starting point is to establish the stable structures and chemical states of the different catalyst components during SCR conditions. This includes [11] high temperatures (200-500°C) and most importantly, the presence of oxygen (∼10%) and water (∼6%) that are believed to influence the catalyst surface morphology. Furthermore, the performance of the catalyst is often correlated to the loading of silver [25, 26, 37, 51] where high NO_x conversion with HCs is reported with 2-4 wt.% Ag. At this point, a fair amount of both small Ag species and large particles are formed [38–40, 141, 142]. In the regime of large particles (5-20 nm) it is most likely that the equilibrium particle shape is based on a Wulff-construction, exposing common low surface-energy facets. As Ag(111) is the stable surface of silver, it is expected to dominate silver crystallites [143]. However, owing to the presence of O_2 during NO_X-SCR it is probable that Ag is oxidized.

4.1.1 Oxidized Ag

The subject of Ag oxidation is covered extensively in the literature [106, 109, 110, 144–167] from both a theoretical [106, 150, 152, 157, 158, 165, 166] and an experimental [144,145,148,149,151] point of view, mainly in connection to oxidation reactions such as methanol to formaldehyde, and ethylene to ethylene epoxide over silver supported on α-alumina. In particular, it is suggested that the oxidation activity is associated with oxide-like surface reconstructions of silver. However, despite numerous studies and attempts to characterize the stable Ag-O phases (oxidized surfaces, surface oxides, bulk oxides) the detailed structural information remained under investigation for more than 30 years. Initial reports by Rovida *et al.* [168] suggested an oxygen induced $p(4\times4)$ reconstruction of Ag(111). Later, using STM measurements and DFT calculations a surface model with a $Ag_{1.83}O$ stoichiometry was proposed [169] based on the structure of $Ag_2O(111)$. However, recent findings [109, 110] show this not to be correct as the stable model presents no resemblance the oxide phase of Ag. Instead, the configuration consists of an $Ag_{12}O_6$ overlayer with two silver hexamer subunits, still in a $p(4\times4)$ periodicity. The structure is shown in Fig. 4.2 (a) where also the Ag $3d_{5/2}$ photoe-

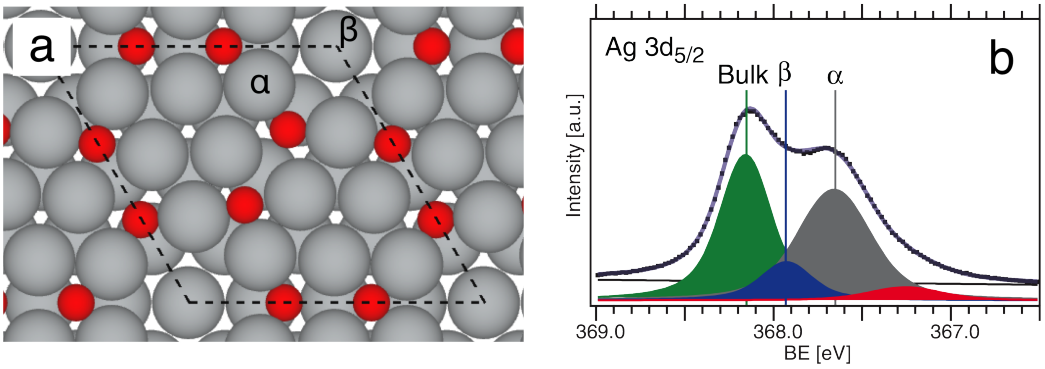

Figure 4.2: a) Ball model of the $p(4\times4)$-O/Ag(111) structure presented in Refs. [109, 110]. O (Ag) atoms are colored red (grey). b) The Ag $3d_{5/2}$ photoemission spectra associated with the structure in (a). Ag atoms assigned to α and β components are indicated in (a).

mission spectra is given. However, under specific preparation conditions, in particular when using atomic oxygen, measurements also show [167] a set of other, coexisting oxide structures, *e.g* with $p(4\times5\sqrt{3})$rect, $c(3\times5\sqrt{3})$rect, or $c(4\times8)$ periodicity and a puzzling "striped" phase which is believed to contain a higher oxygen content ($\sim$0.8 ML) [167]. The particular chemical properties, and structures of these phases are of great interest in the context of lean NO_X reduction over Ag/Al_2O_3 as they potentially could be present on the silver crystallites. In Paper 1, combined HR-XPS measurements and DFT calculations were used to study and characterize these structures, with focus on the high coverage ($>$ 0.5 ML) $c(4\times8)$ and striped structures. By comparing

measured and calculated core level signatures, complemented with STM simulations and thermodynamical stability, the c(4x8) model previously suggested by Schnadt *et al.* [167] was confirmed. However, despite a good match to the experimental photoemission shifts, and previous STM measurements, no thermodynamically stable atomic structure of the striped phase was obtained. Instead, the experimental and theoretical SCLSs suggested presence of a silver oxide phase. Nevertheless, as the different surface reconstructions displayed similar core level shifts as well as thermodynamical stability and local configuration, it seems unlikely that the chemical properties of different Ag-O surface structures will differ to a large extent. In particular, as the measured core level binding energies hold an unique signature for each element [170] they contain information on local atomic environment. For Ag, oxidation leads to negative shifts as compared to the bulk, as observed in Fig. 4.2 (b) for the $p(4\times4)$-O/Ag(111) structure. The Ag atoms denoted α have higher coordination to O atoms than Ag atoms in the furrows (β) and display larger shifts with respect to the bulk component. The deconvoluted red feature in the spectra is assigned to a coexisting, more oxidized phase. The higher the oxidation, the larger is the shift [144, 151, 171–174]. It can be noted that these shifts are reversed with respect to other metals, which show positive shifts upon oxidation, *e.g.* oxidation of palladium results in Pd $3d_5/2$ signatures located at higher binding energies. Understanding the origin of the reversed shifts of Ag can prove important for the particular properties of silver on the basis of the electronic structure.

In Paper 2, the long-standing question of the reversed Ag 3d core level shifts upon oxidation (towards lower binding energies) was elucidated and indeed the results can be used to explain the character of silver reactivity. In a simple electrostatic picture [175], the sign (and to some extend size) of the core level shifts can be correlated to the net atomic charge as (ionic) bonds are formed. In Ag_2O, Ag is cationic and thus positive shifts are to be expected with respect to the metallic Ag bulk. However, this simple model has proven wrong on several occasions [176, 177] and a more detailed picture is necessary. The shift in the binding energy of the photoemitted core electron (E^{CLS}) can be represented by:

$$E^{CLS} = \Delta E - \Delta E^r, \tag{4.2}$$

where ΔE is the change in the on-site electrostatic potential, often referred to as initial state effects, and ΔE^r represents the electronic relaxation around the core hole, *i.e* final state effects. Calculations of the Ag 3d and Pd 3d shifts were performed at different levels of oxidation and the subsequent analysis of the initial state effects (position of the d-band center) as well as the valance electronic structure shows that silver is insensitive to oxidation despite a substantial charge transfer from Ag to O. In Fig. 4.3, selected data from Paper 2 is presented for Pd and Ag. In particular, the structural models for O adsorption (a-d), the calculated core level shifts (e) and changes in the the d-band center (f) upon metal oxidation. For Pd (broken lines), the

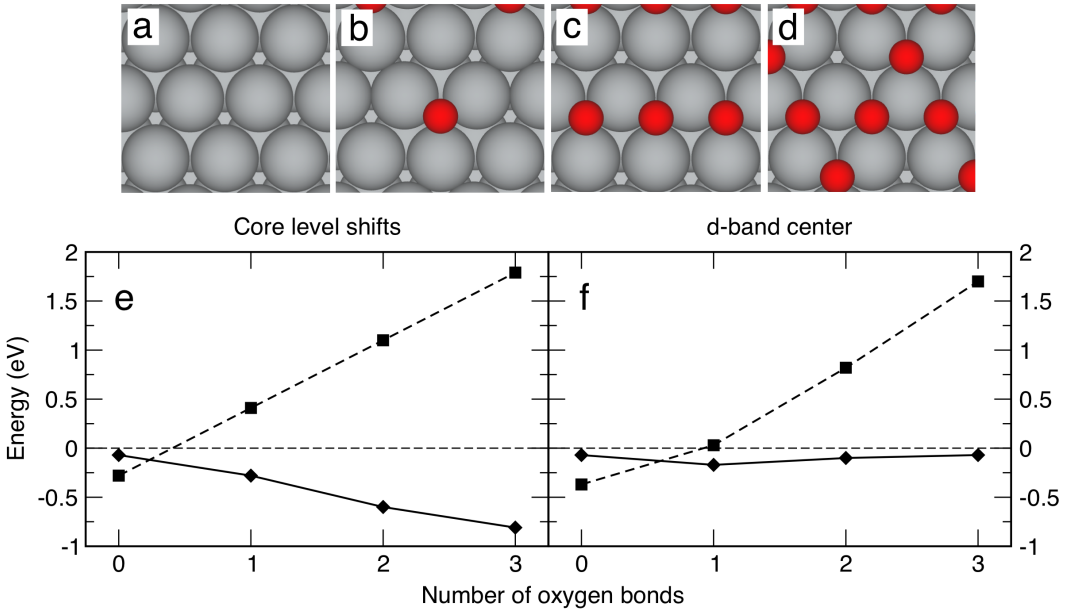

Figure 4.3: Structural models for O adsorption a) clean Ag(111), b) 0.25, c) 0.50, and d) 0.75 coverage. O (Ag) are colored red (grey). Calculated core level shifts (e) and center of d-band (f) are presented for Pd (broken lines) and Ag (full lines). Number of oxygen bonds refers to the coordination of Ag to O.

shifts (e) can be almost entirely coupled to the initial picture, where SCLSs and the position of the metal d-band center (f) are strongly correlated. The origin of the Ag SCLSs (full line) is attributed to the final state where screening of the core hole takes place in bonding states of sp-type. The results clearly displays the sp-nature of silver where bonding and consequently chemical reactivity of the metal is associated the spatially delocalized 5s electrons and an "inert" d-band. In ionic bonds, such as oxidized silver phases, the location and width of the d-band remains virtually unaffected. In hindsight, these results can be used to explain the oxidative properties of silver. Any silver(-oxide)-catalyzed reaction that leads to formal reduction of the metal occurs on the basis of increased occupation of sp-derived metal bonding states.

4.1.2 Reactivity of Oxidized Ag

The subject of Ag reactivity and, in particular, the initial stages of oxidation, *i.e.* O_2 adsorption, can be discussed in light of the Newns-Anderson [178] (NA) and the simpler Hammer-Nørskov [179–181] d-band model that has proven useful in qualitative understanding of chemisorption but also the difference in chemical properties of materials. At this point though, the discussion is limited to the electronic structure effects, but it is important to emphasize existence of structural effects, that will discussed later in

this section. The d-band model is an attempt to understand adsorbate-adsorbent interactions in terms of Molecular Orbital theory. Within the model, coupling of adsorbent and adsorbate electronic states is correlated to their relative position (in energy). In particular, the position of metal d-states, with respect to the Fermi energy, is considered and used as a measure of reactivity. In the case of O_2, also applicable to *e.g.* H_2, CO, and NO, the strength of the adsorption over metallic Ag is derived from a large coupling to the d-states which is promoted by a d-band at higher energies (closer to Fermi). For Ag, however, top of the band is calculated to be at $\sim$ -3 eV (Paper 2). Consequently adsorption of O_2 over Ag(111) is weak. Within the LCAO and PWPP implementations considered in this thesis, the adsorption energies are calculated to be -0.17 and -0.20 eV, respectively. However, in the presence of subsurface oxygen (O_{sb}), defects or other impurities near the Ag(111) surface, Xu *et al.* [163] have shown that adsorption energies of H, C, N, O, O_2, CO, NO, C_2H_2, and C_2H_4 and dissociation barriers of O_2, H_2m and NO can be lower. The increased reactivity was attributed to an induced shift of the silver d-band owing to the presence of O_{sb} and consequently larger coupling to adsorbate states. In this thesis, however, effects of subsurface oxygen has not been considered. Consequently, only minor changes of the electronic structure of Ag are observed as compared to the clean Ag(111) surface. Owing to the weak adsorption energies of O over low-energy silver facets oxidation reactions occur readily.

4.1.3 CO and NO Oxidation over Oxidized Ag

In Papers 3 and 4 oxidation of CO and NO was investigated and found to be highly facile over a model silver surface oxide. In both cases, the stable $p(4\times4)$-O/Ag(111) reconstruction, shown in Fig. 4.2 (a), was considered.

The oxidation of CO to CO_2, is a common model reaction in surface science experiments and calculations which often proceeds via a Langmuir-Hinshelwood scheme. For example, on Pt(111), the CO_2 formation at low CO coverage is measured to be an activated process with a barrier of $\sim$1 eV [182]. On the oxygen induced surface reconstruction of Ag(111) CO adsorption was weak over Ag and the the barrier for CO_2 was calculated to be only 0.28 eV (Paper 3). Subsequent formation of a carbonate specie was calculated to be highly exothermic with a low barrier. Furthermore, the theoretical results are in excellent agreement with the experimentally observed carbonate formation at low temperature (100 K) CO dosage. At room temperature (RT) experiments, however, no carbonate formation was observed. This is consistent with the low adsorption energy of CO_2, which consequently desorbs before reacting with O to form CO_3^{2-}.

Similar results were obtained in the case of NO adsorption over $p(4\times4)$-O/Ag(111) (Paper 4) where the initial barrier for surface nitrite formation was found to be intrinsic and estimated to 0.58 eV. This was consistent with the experimental findings where no

nitrates could be observed at 100 K. Instead, the measured low temperature photoemission shifts were best correlated with NO dimerization. At RT, the recorded N 1s and O 1s spectra indicated a complex interconversion between adsorbed NO_X species, that with increasing NO pressure, could be rationalized with partial decomposition of surface nitrates to nitrites and subsequent NO physisorption, leading to formation of N_2O_3-like structures.

For CO as well as NO adsorption, the uniqueness and close relation of photoemission shifts and the changes in the local atomic environment provided a rare opportunity to understand the carbonate and nitrate formation. In particular, the collected spectra suggest a reconstruction of the initial $p(4\times4)$-O/Ag(111) surface and formation of epitaxial CO_3 and NO_3 overlayers where the XPS peak intensities indicated that nearly all surface oxygen was bound in carbonates/nitrates. The structures and the corresponding C1s/N1s and O1s spectra before (bottom) and after CO/NO exposure (bottom) are shown in Fig. 4.4. Before exposure, no signatures of carbonates and nitrates can be seen in the C1s and N1s spectra and a clear signature of oxygen in the $p(4\times4)$-O/Ag(111) can be observed at 528.4 eV in the two O1s spectra. However, as CO/NO reacts, the oxygen signature at 528.4 disappears and peaks assigned to carbonates and nitrates (and NO) are observed in all corresponding spectra. It should be noted that the CO and NO data were taken at 10^{-6} and 0.01 mbar and temperatures of 100 and 300 K, respectively. Owing to the higher pressure during NO exposure, there is considerable amount of contamination on the $p(4\times4)$-O/Ag(111) surface prior to the NO measurements. This is observed in the O1s spectra around 531 eV. In the case of carbonates (Paper 3), the Ag $3d_{5/2}$ shifts also indicated presence of a highly oxidized Ag specie on the surface (CLS = -0.95 eV). In Fig. 4.4, the specie is marked with a ring. This unique signature, was a key factor when constructing the Ag(111) reconstruction with a carbonate monolayer. In the case of nitrates (Paper 4), the initial surface geometry was based on that for carbonates, but it was later revised, due to an inadequate match to existing STM measurements. Instead, guided by simulated STM and XPS signatures, a modified $p(4\times4)$-NO_3/Ag(111) surface was suggested, seen in Fig. 4.4 (right). The new structure was found to be preferred by -0.20 eV as compared the surface geometry with carbonates.[1] The difference between the two surface structures are the positions of surface carbonates/nitrates within the $p(4\times4)$ cell were the proposed configurations can be viewed as a Ag(111) surface with three point vacancies in each surface cell, each occupied with a carbonate/nitrate molecule. Using bulk Ag as a reservoir, the number of Ag atoms in the reconstruction was allowed to vary. A reasonable question is the validity of this assumption as Ag atom diffusion in the bulk is associated with barriers and the experiments are performed at relatively low temperature. The process is justified by comparison of the free energy of carbonate/nitrate

[1]In hindsight the carbonate structure was considered in a surface geometry based on that for nitrates. The two structures were found within 0.05 eV.

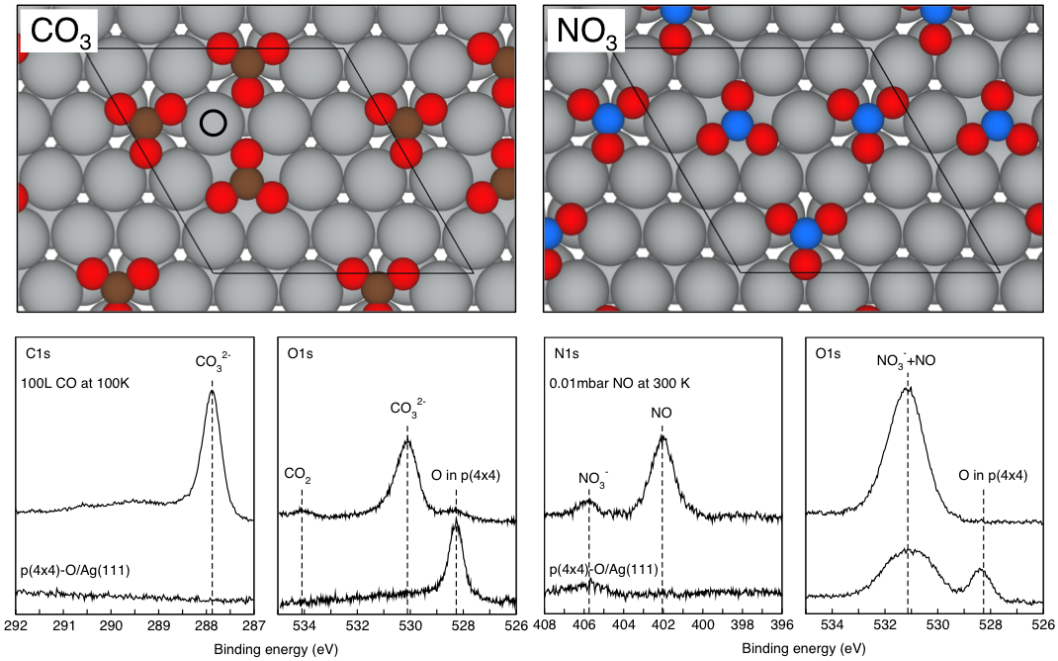

Figure 4.4: The calculated structures with a carbonate (CO_3) and nitrate (NO_3) overlayer. Color codes: C (brown), N (blue), O, (red), and Ag (grey). The $p(4\times4)$ is indicated. For reference, the C 1s, N 1s and O 1s spectra are shown in the bottom panels for the clean $p(4\times4)$-O/Ag(111). Moreover, the spectra are presented after exposure of the $p(4\times4)$-O/Ag(111) surface to 100 L of CO (at 100 K) and 0.01 mbar of NO (at 300), respectively.

formation (-2.63 eV/CO_3 and -1.59 eV/NO_3), and the Ag bulk cohesion energy, which is calculated to 2.50 eV.[2] The difference between the structures containing carbonates and nitrates is the relative position of the vacancies. It is worth mentioning that in both cases, formation of higher order CO_X and NO_X species results in formal reduction of the Ag surface. In the initial stage, the $p(4\times4)$-NO_3/Ag(111) structure holds six oxygen atoms, each formally in a -2 state. Hence, the oxidation state of the $p(4\times4)$ structure is -12. With formation of carbonates (CO_3^{2-}) or nitrates (NO_3^-) the surface is reduced, as observed in the measured and calculated photoemission spectra.

4.1.4 Oxidized Ag_n Clusters

Thus far, only the state and reactivity of Ag atoms originating from the pristine low energy (111) orientation have been discussed. In general, however, metal crystallites contain atomic steps, kinks, corners, row-reconstructions, impurities, and defects where the

[2]Note that three carbonates/nitrates are formed per $p(4\times4)$ where only diffusion of one Ag atom is necessary.

average coordination, *i.e.* number of nearest neighbors, is lower as compared to terrace atoms. Consequently, these special sites have a more narrow and shifted d-band [183] (towards Fermi) with increased reactivity (higher adsorption energies). These are often referred to as geometrical effects and in many cases the catalyst activity is directly proportional to the amount undercoordinated sites, for example during synthesis of ammonia [184]. Based on these, and other similar findings, it is often suggested that a metal particle based catalyst should be formulated such as to increase the active metal surface area, maximizing the number of active sites and hopefully activity. Realization of such a catalyst consequently implies a high dispersion of the metal particles. However, as the particles size is reduced to the region of cluster phase, averaging few nanometers (or even Ångtröm) in size, the question of finite size effects becomes highly relevant.

It is often suggested that the activity in alumina is associated with presence of small Ag_n (n = 1-10) clusters, indicated by UV-vis and EXAFS measurements [38, 39]. In the literature, Ag clusters are suggested to promote selectivity towards NO_X reduction under lean conditions [35, 52, 185–187]. In order to clarify the the role of Ag clusters, it is necessary to investigate the size-dependent catalytic reactivity, and stability of Ag in the smallest, sub-nano regime, in the presence of oxygen in particular. However, despite all work related to extended Ag surfaces, little information is available on the oxidation of small silver clusters. General geometrical and electronic character of Ag_n clusters have been addressed [188–190], as well as oxygen adsorption on small silver clusters [147, 191–201]. However, the question as to how the catalytic and adsorption properties of silver change with reduced size has not been considered. As average coordination in small cluster is significantly lower than in the corresponding bulk phase, one could assume that the clusters are more reactive than the corresponding bulk. However, this should be investigated explicitly as properties such as ionization potentials [202, 203], electronic affinities [204], magnetic moments [205], and reactivity [206, 207] may change from one cluster size to another. Electronic and geometrical structures are closely coupled at the sub-nano scale. In Paper 5, it is shown that the geometrical shape of neutral Ag_n clusters ($n < 10$) can be directly linked to the electronic structure of the clusters. The results are rationalized by formation of shell closings that originate from spatial confinement of electrons and subsequent spin pairing in electron levels [208–212]. Again, mainly the 5s electrons contribute to chemistry, and any bonds that are derived from interactions between these electrons, constitute delocalized states over the clusters, leading to shell closings: 1S, 1P, 1D, 2S, 1F etc. corresponding to 2, 8, 18, 20, 34 etc. electrons. In the size interval considered in Paper 5, this implies a high stability, and low reactivity, for the dimer and octamer.

Hence, also for small Ag clusters, oxidation appears to be a competition between silver to oxygen charge transfer and Ag-Ag cohesion. This is clearly illustrated in Fig. 4.5 where the thermodynamical stability is a direct consequence of this competition.

[3] Fig. 4.5 shows that Ag_2O (bulk oxide) is the stable bulk phase of silver (in the

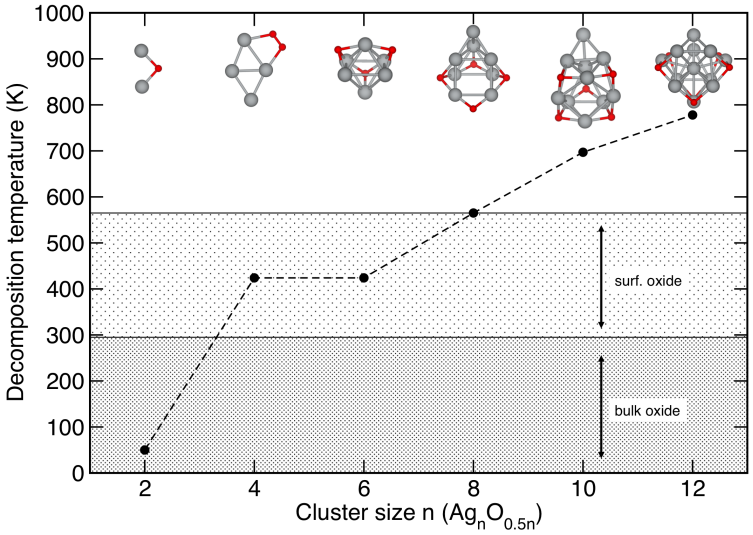

Figure 4.5: Relative thermal stability of stoichiometric clusters, the bulk and oxidized surfaces of Ag(111). The insets show the stable structures for $Ag_nO_{0.5n}$. In addition to the clusters considered in Paper 5, the stoichiometric decamer and dodecamer clusters are presented. Color codes: O (Ag) in red (grey). The decomposition temperature is considered at an O pressure of 0.001 atm.

presence of oxygen) at low temperatures. The bulk oxide decomposes around 300 K, forming oxidized surface reconstructions of silver. The oxygen coverage of these surfaces decreases with increasing temperature. At 590 K, and above, the calculations suggest that metallic Ag(111) is stable phase of silver. The thermal decomposition of oxidized, stoichiometric Ag_n clusters is calculated as the temperature at which O_2 desorbs, *i.e.* $\gamma = O$ (3.6). In general, the stability is calculated to be size dependency. The results can be understood from from the electronic structure. For small clusters, cohesion originates from delocalization of electrons, forming jellium-like states. Dissociative adsorption is associated with substantial charge transfer from the metal to oxygen, formally four electrons per oxygen molecule. This type of adsorption is better accommodated on larger clusters and extended Ag systems where charge transfer and formation of local ionicity, as a consequence of oxygen adsorption, can be efficiently screened. As a consequence, the larger clusters and the extended systems display higher oxygen adsorption energies and thermodynamical stability. Oxidation of clusters, at least partial oxidation, is favorable as long as some Ag cohesion is maintained. This is the case in *e.g.* the tetramer and the hexamer. Hence, formal oxidation through dissociation and consecutive O adsorption is a balance between metallicity and ionicity.

[3]To enable direct comparisons between theoretical and experimental stability, all energies have been corrected to reproduce experimental O_2 and Ag-bulk binding energies of 5.17 and 2.80 eV [108,213], respectively.

The results show that despite lower average coordination, the reactivity and towards oxygen adsorption is lower over the small clusters owing to finite size effects. Thus, the oxidation reaction, NO_X to NO_{X+1}, is calculated to occur readily over the clusters, in similarity with the extended surfaces.

Besides providing direct sites for catalytic reactions, it is often speculated that supported metal particles and clusters could lead to formation of special sites at the metal-substrate interface region. This has theoretically been shown for Au particles [214–216] over MgO and TiO_2. Increased reactivity could also be attributed to "thin film effects" where oxide induced polarization in the monoatomic metal layer leads to higher adsorption energies [217]. If the reactivity of Ag/Al_2O_3 is primarily associated with the existence of small Ag clusters and the formation of interface regions, then this issue needs special attention in the case of silver supported on alumina. However, before addressing this subject, a short review on the atomistic modeling of γ-alumina is needed.

4.2 Modeling Ag/Al_2O_3

Using traditional experimental methods, *e.g.* IR [54, 121], XRD [55], TPD [122], EELS [123], and NMR [56,124], electronic and structural properties of γ-alumina have been investigated. Based on that information, several atomistic models for γ-alumina have been put-forth in the literature [218–222]. In this work, the spinel structure proposed by Digne *et al.* [223] has been used. The model has been employed on several occasions [55, 223–225] and calculated properties, such as thermodynamical stability and vibrational frequencies of adsorbates (CO and OH) are in good agreement with experimental findings. Moreover, with the correct acid-base properties and perhaps even local structure and coordination, it is possible that the model proposed by in Digne *et al.* [223] could be of relevance when modeling γ-alumina systems.

In experimental situations, any local changes in material electrostatics, due to *e.g.* doping or defects, are compensated and stabilized by a long-ranged response of the surrounding atoms. However, as theoretical atomistic modeling involve size-restricted models, any induced changes to the slab structure need "manual" care, as is the case for the Ag/Al_2O_3 model presented in Paper 4. The bonding in alumina is ionic between Al^{3+} cations and O^{2-} anions. For charge neutrality, the Al_2O_3 slab needs to be modeled such as to sustain the stoichiometric 2:3 conditions. However, when one Al atom in the alumina matrix is replaced by the monovalent Ag, the overall balance between supply and demand of electrons is disturbed. The supercell is, so to speak, two electrons "short", and due to lack of global stabilization, the model surface slab might present unrealistic properties as initially non-existing electronic states, and electrostatics are induced. The solution, although crude, is simple and effective. By compensating every "missing" electron by a H-atom, adsorbed somewhere on the slab, the charge neutrality

as well as bandgap are kept. In Fig. 4.6 (a) the total density of states if presented for the bare Al_2O_3 surfaces, along with local DOS for the different dopant atoms: Ga (b) , Y (c), Ag (d), and Ag compensated with two H (e). Gallium and Yttrium are both tri-valent and although they impose local structural changes, no evident discrepancies in the electronic structure are observed. The bandgap is kept close to that of clean alumina. In Fig. 4.6, also the atomic model of the "compensated" structure shown in

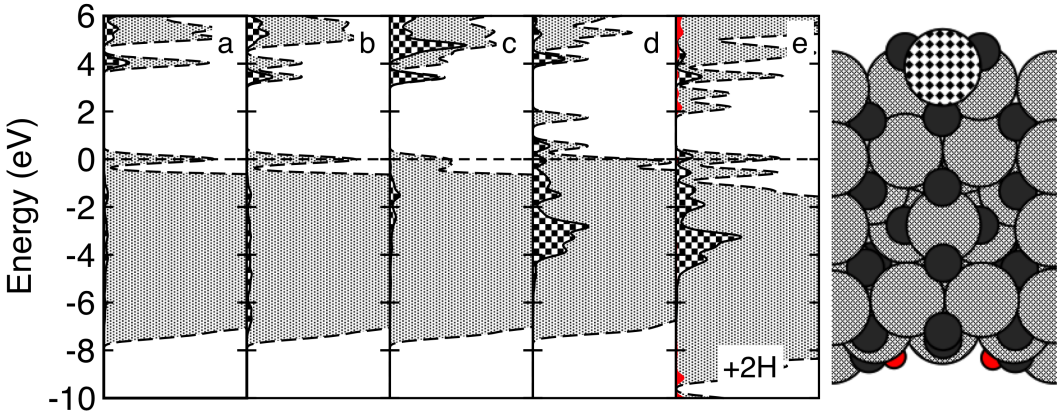

Figure 4.6: The densities of states of bare alumina (a), with a Ga dopant (b), with an Y dopant (c), with an Ag dopant (d), and finally with an Ag dopant but stabilized by two H atoms (e). The local DOS for the respective dopant atoms (checked), and additionally on hydrogen (red) is also displayed. In the case of bare alumina (a), the projection is done on the Al atom at the dopant position. All energies are aligned to the Fermi level. Also the atomistic model of the "compensated" system system is presented. Color codes: H (red), O (black), Al (grey), Ag (checked).

a side view. However, when aluminium is substituted for Ag, a monovalent s-metal, states are induced at Fermi that could lead to different chemistry. By compensating the system with two hydrogen atoms, the bandgap is restored.

4.3 Reactivity of Ag and Ag/Al_2O_3

In the case of Ag(111) and $p(4\times4)$-O/Ag(111), low adsorption energies are calculated for molecular chemisorption of CO (Paper 3), NO (Paper 4), O_2 (Paper 5), and H_2 (Paper 6). Moreover, high barriers for O_2 and H_2 dissociation are found over Ag(111) the Ag_n clusters. However, as these studies mostly include well defined Ag(111) reconstructions and gas-phase clusters, it is reasonable to question the transferability of these results to the Ag/Al_2O_3 system, containing interfaces and interaction effects between the alumina and the silver. One possible route to rationalize these effects and probe the reactivity of Ag/Al_2O_3 can be via the changes in the electronic structure, and in particular the Ag d-band center as silver-alumina interfaces are formed. If the

interactions between the two components are strong, the changes to the Ag density of states (as compared to the corresponding gas-phase structure) should be observable. For that reason, Fig. 4.7 presents the calculated low-energy structures of Ag in different phases: nanoparticle (NP), Ag_{10}, and Ag_1 cluster over $Al_2O_3(100)$. To follow the changes in the electronic structure the corresponding DOS is presented. The total DOS (Ag and Al_2O_3) is shown in black. Moreover, projections are made onto Ag d- (grey), p- (orange), and s-states (broken red). The important results are observed in DOS diagrams (E)-(L), however, for reference, also the clean $Al_2O_3(100)$ [A] and Ag at different levels of oxidation: (B) full [$Ag_2O(111)$], (C) partial [$p(4\times4)$-O/Ag(111)], and (D) no oxidation [Ag(111)] are displayed. In general, with reduced level of Ag oxidation the characteristic delocalization of sp-derived states is observed and the d-band narrows and shifts towards lower energies. In (E), (F), and (G) the DOS is presented for the gas-phase structures of Ag_{NP}, Ag_{10}, and an Ag atom, respectively. Notably, the electronic structure in (E) and (F) is similar to that of Ag(111) (D), suggesting that these systems could have comparable reactivity.[4] In order to investigate the effects of the Ag-alumina interface these three Ag structures are supported on the $Al_2O_3(100)$ surface. However, the the corresponding projected DOS, shown in (H), (I), and (J) for $Ag_{NP}/Al_2O_3(110)$, $Ag_{10}/Al_2O_3(110)$, and $Ag/Al_2O_3(110)$, respectively, are very similar to those of the gas-phase counterparts [in (E), (F), and (G)]. The PDOS of the Ag nanoparticle (H) shows that the metallic Ag interacts weakly with the alumina support as also the d-band center remains virtually unaffected. By comparison with the $p(4\times4)$-O/Ag(111) (C) and the clean Ag(111) (D) surface it can be concluded that the alumina supported Ag nanoparticles can be modeled by extended low energy facets. However, this observation is not general and at this point only restricted to Ag particles and attributed to a low lying 4d-band and delocalized 5s electrons that efficiently can screen any effects of the substrate. For $Ag_{10}/Al_2O_3(110)$ (I) and $Ag/Al_2O_3(110)$ (J), interactions with the support takes place in the Ag sp-levels with some minor changes of the electronic structure, primarily by a small shift and broadening of the d-states. Summarizing, the electronic structure of considered Ag phases suggests that the formation of interfaces has minor effect on the electronic structure.

However, as some literature suggests presence of sliver-aluminate phases [29, 31], the clusters, Ag_{10} (K) and Ag atom (L), are also considered when anchored in the alumina matrix. This is performed by creating an Al vacancy and and putting the silver atom into the defect. In both cases, (K) and (L), the electronic structure shows a larger broadening and shift of Ag d-states (towards Fermi) as compared to the supported structures [(I) and (J)], indicating that also the d-electrons could be involved in hybridization and bond formation to the surface. The results suggest a a larger extent of Ag oxidation and consequently higher chemical reactivity for anchored species.

[4]The Ag_{10} has s-derived jellium states (in red), and the reactivity could also depend on the particular symmetry of these states.

In summary, the investigation of the electronic structure predicts weak interaction

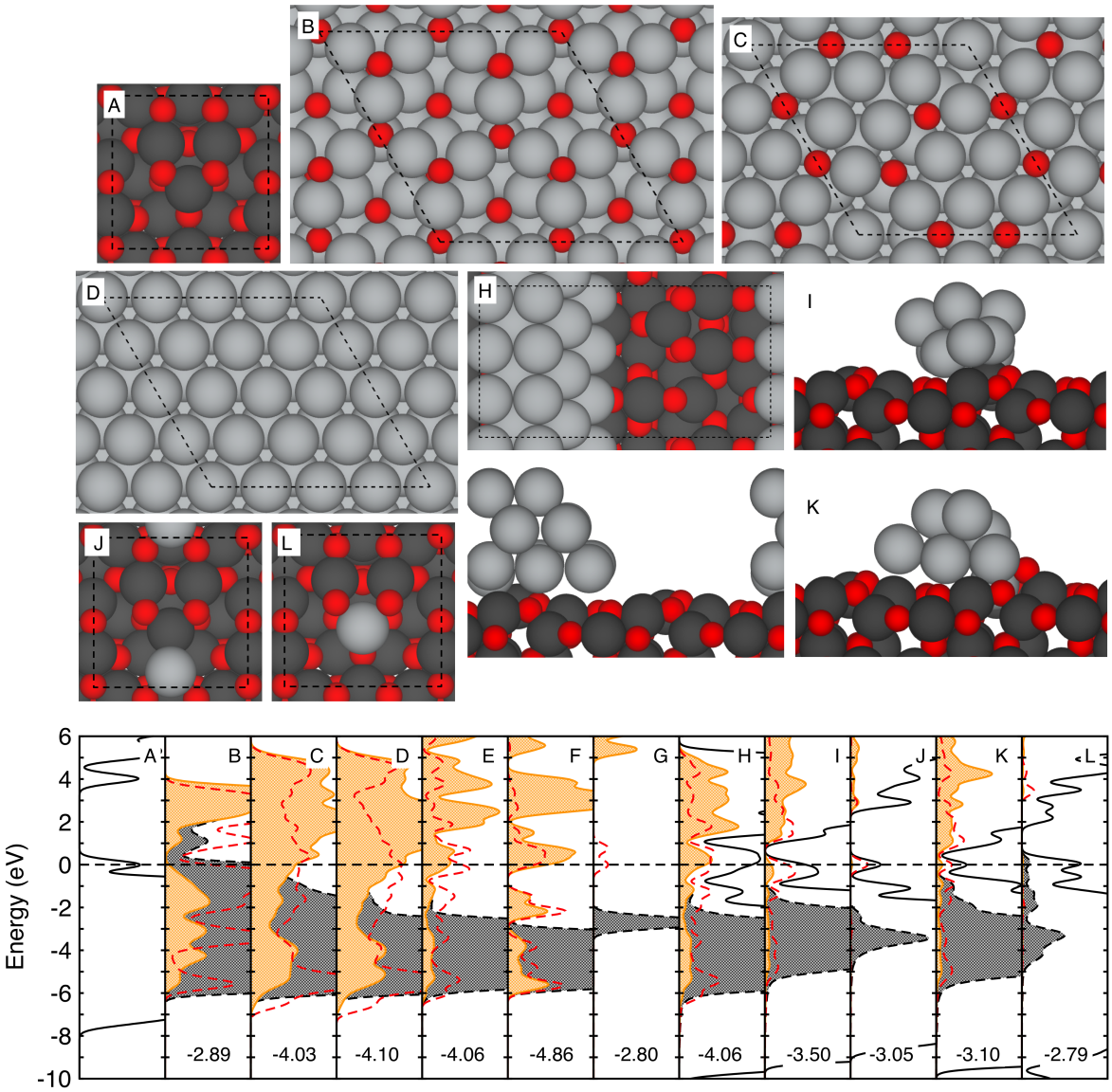

Figure 4.7: Total density of states (full black line) and projections on Ag s- (red broken line), p- (orange), and d-states (grey). Fermi energy is indicated at 0 eV. (A) $Al_2O_3(110)$, (B) $Ag_2O(111)$, (C), $p(4\times4)$-O/Ag(111), (D) Ag(111), (E) Ag_{NP} (gas-phase), (F) Ag_{10} (gas-phase), (G) Ag atom (gas-phase), (H) $Ag_{NP}/Al_2O_3(110)$, (I) $Ag_{10}/Al_2O_3(110)$, (J) $Ag/Al_2O_3(110)$, (K) $Ag_{10}@Al_2O_3(110)$, and (L) $Ag@Al_2O_3(110)$. The d-band center is given in eV. The corresponding structures are shown for (A)-(D) and (H)-(L). In the case of (E), (F), and (G) the structures are the gasphase Ag components presented in (H), (I), and (J), respectively. Color codes: O (red), Al (dark grey), Ag (grey).

between supported Ag and Al_2O_3, with only minor effects of the metal-substrate interface. However, if Ag clusters are anchored to the surface there are observable changes

in the PDOS, similar to those observed during oxidation of gasphase Ag_n (n = 1-9) clusters (Paper 5), which were found to be reactive for NO_X oxidation reactions. Also, H_2 adsorption and dissociation is found to be similar over Ag(111) (D) and supported Ag nanoparticle (H), presumed to be metallic, while dissociative chemisorption of H_2 takes place over $Ag@Al_2O_3(110)$ (L) (Paper 5).

The reactivity of the different Ag phases has been discussed on the basis of the electronic structure, and to some extent, the d-band model. However, a small note of caution is needed with respect to the d-band picture. Within the general assumption, the contribution of the sp-band is assumed constant. Hence, changes are the reactivity is directly correlated with changes in the d-electrons. For small clusters however, this is not necessarily true. Based on laser ionization and MS measurement in combination to DFT calculations, Holmgren *et al.* [226] showed that size dependent variations of the CO adsorption energy over Cu_n (n=15-21) clusters mainly originates from differences in sp-contributions. The d-contribution varies also, but to a smaller extent. Consequently, to a certain approximation, for small free electron metal clusters such as Cu_n, Ag_n and Au_n the reactivity is correlated with changes in the sp-band, *i.e.* the jellium states. Formation of these states, will generally affect several electronic properties, such as ionization potentials (IP) and adsorption energies. As these properties have clear size dependent odd-even alternation (Paper 5), the position of e.g. HOMO from one size to another could move. As the projected DOS plots for clusters, in Fig. 4.7, are presented with respect to the Fermi energy (taken at HOMO-level) the absolute position of the different states (d, s, and p) could, in fact, be different with respect to a constant energy reference, say the vacuum level. Thus, the position of the d-band can vary with cluster size and, on the same argument, differ for isomer structures. In the case of extended systems, bulk and surface slabs, this effects is minor as the silver d-band remains constant for the bulk.

If Ag exists in/on the Ag/Al_2O_3 catalyst with varied size and oxidation level, defining an appropriate descriptor can be difficult. As the d-band is largely affected by size effects probably another descriptor is more suitable. However, during HC-SCR, the NO_X reduction reactivity is highly influenced by the reducing agent. This suggests that the different reactions and even the rate determining step (RDS) can shift. As there is no general agreement as to what the RDS, or steps, can be, it seems unlikely that the d-band model can be applied to connect the different reactions and intermediates.

	α^a	d^b_{Ag-C}	d^b_{C-O}	E^c_{ads}	ω^d	$\pm\Delta\omega^d$
CO	-	-	1.14	-	2117	0
Ag_4	linear	2.05	1.15	-0.90	2046	-71
Ag_4^+	linear	2.13	1.13	-0.85	2139	+22
O_2/Ag_4	141	2.17	1.15	-0.72	2049	-68
$4O/Ag_8$	linear	2.18	1.14	-0.40	2114	-3
Ag(111)	linear	2.17	1.15	-0.24	2038	-79
$p(4\times4)^e$	159	2.45	1.15	-0.23	2093	-24
$Ag_2O(111)$	linear	2.03	1.14	-0.67	2111	-6
$Ag@Al_2O_3$	169	2.05	1.14	-0.81	2138	+21

Table 4.1: [a]The Ag-C-O angle. [b]Bond lengths measured in Ångström. [c]The adsorption energy in reference to CO in the gas phase (eV). [d]The calculated vibrational frequency in cm^{-1}. [e]The $p(4\times4)$ refers to the $p(4\times4)$-O/Ag(111) surface. The corresponding structures for Ag(111), $p(4\times4)$, $Ag_2O(111)$, and $Ag@Al_2O_3$ are shown in Fig. 4.7.

4.4 Probing the Structure and Chemical Properties of Ag/Al_2O_3

4.4.1 CO Adsorption

A possible route to understand the individual components and the combined Ag/Al_2O_3 is by using a probe molecule. In this context, CO is often used. In fact, the study presented in Paper 3, originates from an idea to use CO as a probe molecule to investigate oxidation of silver in the Ag/Al_2O_3 catalyst. The reason was the link between CO vibrational frequency and the amount of charge transfer between CO and the metal [202]. Donation from the HOMO [227] level of CO (5σ) to the metal LUMO level is accompanied by shortening of the C-O bond, with a general blue-shift in vibrational frequencies. Back-donation on the other hand, is related to filling of the CO antibonding $2\pi^*$ state, generating repulsion between C and O and consequently longer bond distances and red-shifted CO vibrational frequencies. Utilizing the CO response of the adsorption site, a possibility could be to track the level of oxidation [228]. In Tab. 4.1, a summary of the computational results is presented [229]. In general, adsorption on Ag in a higher oxidation state displays more donation and blue shift of the vibrational frequencies in reference to the gas phase. On the O_2/Ag_4 cluster, where molecular oxygen is adsorbed, the CO frequency displays no shift as compared for the neutral Ag_4 cluster. However, when adsorbed on the cationic Ag_4^+ cluster the shift is large and "blue" and the C-O bonding distance is shortened. On the thermodynamically stable $4O/Ag_8$ cluster (Paper 5), the CO frequency shift is calculated neutral with respect to gas phase CO trial (-3 cm^{-1}). Adsorption on Ag(111) displays a clear back-donation signature with a "red" vibrational frequency shifts (-79 cm^{-1}) and prolonged bonding distances as compared to the gas phase (1.15 Å). Oxidation of

the Ag(111), towards the stable oxidized surface reconstruction, $p(4\times4)$, and finally the fully oxidized $Ag_2O(111)$ is also displayed in the CO vibrational frequencies with a general trend towards less negative values. Lastly, calculated CO frequency and bond length over an Ag atom embedded in alumina matrix displays a large blue-shift (+21 cm^{-1}) and a shortened bond (1.14 Å). This result suggests that the 5s electron has been stripped from silver and a locally positive Ag^+ is left. In this case, adsorption of CO is largely dominated by donation effects.

Based on the calculated shifts, it seems possible to probe the alumina surface using CO. In particular, if there is presence of cationic Ag (here modeled via Ag_4^+ and $Ag@Al_2O_3$), the shifts are distinctly separated from the other systems. However, our joined theoretical and experimental attempts have indicate that low temperatures ($<$ 100 K) are necessary to clearly differentiate the vibrational signatures.

4.4.2 H_2 Adsorption

Another process, used commonly for educational purposes, often over metal surfaces, is adsorption of H_2. Interestingly, for SCR catalysis it has been shown that hydrogen also has important properties that affect the overall SCR reaction over Al_2O_3. In general, addition of H_2, in small amounts further promotes NO_X conversion with hydrocarbons and shifts the activation to lower temperatures. The origin of the "H_2-effect" is unknown but similar results are observed for NH_3 assisted reduction over silver alumina where almost 90% conversion, already at 200 °C, can be achieved in the presence of hydrogen. The first step in a hydrogen assisted SCR should be H_2 dissociation. In Paper 6, a systematic investigation of this particular process was considered over a representative set of sites over Ag/Al_2O_3. In summary, the calculations showed that dissociation over bare alumina and metallic Ag is associated with substantial barriers. Moreover, based on a nanoparticle model previously used by Molina and co-workers [214–216], no changes in the dissociation energetics were calculated in the presence of the Ag-alumina interface. Instead, low barriers were calculated over Ag-ions in the alumina matrix, and partially oxidized silver [$p(4\times4)$-O/Ag(111)]. The results were rationalized by analysis of the electronic structure (PDOS) within the NA-model. When H_2 adsorbs on Ag(111) and alumina the discrete adsorbate state, bonding and antibonding, fall well below the Fermi energy and consequently the dissociation barrier is high. Over ionic Ag, the adsorbent states are initially higher up (d-band shifted up) and the formed antibonding states depleted. This gives rise to strong chemisorption and low H_2 dissociation barrier.

In general, the results suggest that H_2, most probably, is found in the close vicinity of partially oxidized silver and that H_2-effects is largely absent over bare owing to a high dissociation barrier. Because the dissociation was found similar over extended Ag surfaces and a model nanoparticle, the study also indicates that the catalytic proper-

ties of large Ag particles can be explored on a separate basis, modeled by extended Ag and Ag-O surfaces.

Finally, in the adsorption of CO and H_2 was considered over the surface atoms of alumina in the presence of an Ag ion. The goal was to estimate the effects of Ag doping, owing to induced geometrical and electronic changes, on the reactivity of the surrounding alumina. However, no such effects were observed in adsorption energies, geometries, nor vibrational frequencies of CO and H_2. This suggests that the effects of Ag doping is local and that any increase in catalytic activity, in the presence of Ag, is most probably related to the Ag-phase itself.

4.5 NH_3 Assisted Selective Catalytic Reduction of NO_X over Ag/Al_2O_3

The work in Paper 7 was largely initiated by a recent report from Doronkin *et al.* [50] where it was suggested that the NH_3-SCR activities (already at 200 °C) over Ag/Al_2O_3 and pure Al_2O_3 are similar under fast-SCR like conditions, *i.e.* mixtures of NO and NO_2, and the advantageous effect of H_2 only was observed for Ag/Al_2O_3. In the absence of NO_2, no activity was observed over bare alumina, regardless of H_2 content. These results suggest that the activity over Al_2O_3 is conditional on fast-SCR conditions by NO to NO_2 oxidation. We have calculated that NO oxidation is facile over over partially oxidized Ag (Papers 3 and 5).

With the results from Papers 1-6 at hand, sufficient understanding of the catalyst components and their reactivity was obtained to allow for a more detailed study of NO_X reduction over Ag/Al_2O_3 (Paper 7). In particular, reduction was considered based in NH_3-SCR and performed in view of available sites and components presented in Fig. 4.1. Ag clusters were, however, not considered as the previous studies (Paper 5) could not identify any new catalytic SCR properties associated with the smallest Ag sizes. Moreover, small Ag_n clusters have strongly size-dependent fluctuations in physical and chemical properties. At the present, however, the detailed structure of these clusters in Ag/Al_2O_3 is unknown.

The reaction mechanisms were developed on the basis of previous density functional theory calculations where standard- and NO_2-SCR reaction schemes were considered over V_2O_5 [133–136, 139, 140], H- [137] and Fe-exchanged [138] zeolites. These studies suggested that formation NH_4^+ was a crucial reaction step were reduction occurs via an intermediate formation of nitrosamine (NH_2NO).

Our calculations over an Ag/Al_2O_3 model show that the initial formation of ammonium (NH_4^+) indeed is important for the NH_2NO formation over hydroxylated alumina. The reaction is, moreover, found to be greatly stabilized in the presence of NO_2, *i.e.* fast-SCR stoichiometry. The process proceeds though an Eley-Rideal mechanism and

displays substantially lower energetics than a reduction scheme based on standard-SCR. The results also suggest that the presence of NO_2 reduces ammonia poisoning of the alumina surface with stabilization of ammonium (NH_4^+).

Reduction of NO_X was also considered over partially oxidized [O-p(4×4)] and hydroxylated [OH-p(4×4)] Ag. Over O-p(4×4), Eley-Rideal and Langmuir-Hinshelwood mechanisms were considered, whereas the OH coverage on OH-p(4×4) was found to block the initial NO adsorption and oxidation reaction. The formation of NH_2NO was calculated with low barriers over both surfaces via an Eley-Rideal route. Adsorption of NO and the subsequent formation of stable surface nitrites over O-p(4×4) resulted in high barriers towards a surface nitrosamine. This suggests that one role of H_2 could be to reduce the formation of stable nitrites (and subsequently nitrates) as these species were not formed over OH-p(4×4). However, despite the presence of H_2, it is noted that hydrogen on the Ag surfaces shows no effect in the SCR energetics, indicating that it probably does not actively take part in reduction reactions. Finally, reduction over partially oxidized and hydroxylated silver was calculated to proceed without a precursor ammonium adduct.

For reference, NO reduction over the silver oxide phase, modeled with $Ag_2O(111)$, was considered via an Langmuir-Hinshelwood mechanism and the formation of NH_2NO was calculated with low barriers (0.38 eV). However, owing to the H_2O content during SCR reactions, the surface will probably contain a coverage of hydroxyls that could affect the adsorption of NO and NH_3. At this point, the thermodynamical stability of OH groups and the corresponding structures of hydroxylated $Ag_2O(111)$ have not been established. This could be a relevant theoretical study in order to ultimately determine the charge state of Ag during lean NO_X reduction over Ag/Al_2O_3.

Analysis of the electronic structure and the reaction geometries shows that the surface acidity plays a crucial role. Alumina is hydroxyl-covered and offers little in ammonia dissociation, *i.e.* formation of NH_X species. Thus, the presence of ammonium is found to be important over hydroxylated Al_2O_3, perhaps it even is a rate-determining step. In the case of Ag, the unsaturated, Lewis acidic, Ag atoms in the Ag_6 units of the p(4×4)-O/Ag(111) reconstruction are highly reactive towards NH_3 adsorption. In reaction with NO, the presence of nearby surface oxygen promotes the formation of OH groups and water, which leads to a highly exothermic reaction landscape and low barriers. On the metal, the charge transfer related to formation of bonds, is diluted within the broad bonding resonance while in the oxide (with a large bandgap and no defects) any transfer of electrons between the adsorbent and adsorbate occurs on taking/putting electrons from/in the conduction- or valance band. Without defects or impurities such adsorption is related with high energetic costs. It is possible that small Ag clusters, embedded in the alumina matrix could induce the change to the electronic structure of alumina such as to stabilize *e.g.* ammonium ion formation. This aspect has not been investigated, but calculated adsorption energies and vibrational frequen-

cies of CO adsorbed over $Al_2O_3(110)$ showed minor changes when the alumina surface was doped with an Ag ion. This suggests that effects of Ag are only local, perhaps as local as merely nearest-neighbor atoms.

5 Conclusions and Outlook

HC-SCR over Ag/Al_2O_3 is a promising alternative for lean NO_X reduction. However, as several fundamental issues with respect to the active phase and reaction mechanisms remain unclear, the catalyst development in terms of activity, selectivity, and stability is slowed down and HC-SCR over Ag/Al_2O_3 is still not used for lean NO_X reduction. The experimental and theoretical studies have given a large collection of data which has generated experience as to how the Ag/Al_2O_3 catalyst will perform in terms of activity and selectivity depending on various parameters such as the preparation method, Ag loading, type of reducing agent, and reduction conditions. However, no fundamental breakthroughs have been made so far and the fundamental, atomistic knowledge and understanding about the catalyst and the ongoing reaction mechanisms is largely absent, hindering the design of improved catalysts.

This thesis contains a density functional theory study of lean NO_X reduction over Ag/Al_2O_3. Several fundamental issues are clarified with respect to the Ag component and the reaction mechanisms. The work contains a systematic approach to this particular catalytic system where DFT is initially combined with surface science experiments, based on x-ray photoemission spectroscopy and scanning tunneling microscopy, in order to study the oxidation of metallic silver (Paper 1), understand the chemical signatures (Paper 2), and finally probe the catalytic reactivity of oxidized Ag(111) (Papers 3 and 4). In detail, XPS and DFT were used in Paper 1 to characterize the structures of oxidized silver in the limit of high coverage (> 0.5 ML). Based on agreement of measured and calculated core level signatures, complemented with STM simulations and thermodynamical stability, a c(4x8) surface reconstruction is verified. Moreover, experimental and theoretical SCLSs suggest presence of a silver oxide phase. Comparing the SCLSs and thermodynamical stability of these phases to already established surface reconstructions of Ag(111) shows that the difference in signatures and stability is minor. This suggests that the chemical properties, thermodynamical stability, and local configuration of different Ag-O surface structures are similar.

The relative photoemission signatures of O and Ag are explored extensively in Papers 1-4. However, upon oxidation, Ag shifts are reversed as compared to other metals. The Ag 3d shifts are towards lower binding energies (with respect to bulk). This suggests that the electronic structure of silver is of unique character. Understanding the origin of these shifts can also provide insight on to the catalytic properties of Ag. In Paper 2, calculations were performed in order to separate the initial and final state effects that are believed to contribute to the core electron binding energy. In particular, a comparative study of Pd 3d and Ag 3d CLS was performed. The initial state effects,

often ascribed to changes of the on-site core potential, are shown to be substantial for oxidized Pd, with marked broadening and shift of the Pd 4d-band. For Ag, the on-site core potential is found to be insensitive to oxidation, and consequently the shift in Ag core levels is attributed to final states effects; electronic relaxations around the core hole.

Joint theoretical and experimental studies of low- (100 K) and room temperature CO and NO adsorption on oxidized Ag(111) are presented in Papers 2 and 3, respectively. The measured photoemission spectra of CO/NO dosage indicated CO_3^{2-}/NO_3^- on the surface with subsequent reconstruction and formation of an epitaxial layer with carbonates/nitrates. Calculated potential energy surfaces and core level shifts are used to verify and understand adsorbate oxidation and furthermore clarify the formation process and structures with carbonate/nitrate overlayers.

Having established the structure, stability, and reactivity and reviewed the electronic structure of silver phases at the nano-scale, the aims of Papers 5-7 was to investigate some of the issues that cannot easily be resolved experimentally. In Paper 5, oxidation of small Ag_n clusters ($n < 10$) is considered where low energy structures of molecular and dissociated oxygen are calculated. The electronic and geometrical results of the clean and oxidized clusters are explained via delocalization of 5s electron and subsequent formation of a shell structure. As a consequence of the jellium-like valence states, the calculated adsorption energies of oxygen show pronounced odd/even alternation. Using *ab initio* thermodynamics, we are able to show that the relative stability of oxidized clusters, as compared to that of extended Ag-O phases, in general, is lower. Moreover, the barrier for O_2 dissociation is calculated to be higher over the Ag octamer than an Ag(111) surface. Finally, adsorption of NO and NO_2 onto oxidized clusters results in formal reduction of silver based on nitrite and nitrate formation, respectively.

Several experimental studies indicate that small amounts of H_2 leads to a lower light-off temperature and increased lean NO_X reduction activity over Ag/Al_2O_3 irregardless of reducing agent, *i.e.* NH_3 or HCs. The first step in such a reaction pathway, H_2 dissociation, is investigated with DFT (Paper 6) where relevant Ag phases and possible sites for dissociation are considered. In general, dissociation over metallic Ag phases and bare alumina is calculated to be activated whereas silver-oxide and atomic Ag in alumina display a facile reaction landscape for H_2 dissociation. The effect of the $Ag\text{-}Al_2O_3$ interfaces is shown to be minor with respect to H_2 adsorption energies and dissociation barriers.

Finally, the generated knowledge and understanding from the model studies in Papers 1-4 and the theoretical investigations in Papers 5 and 6, correlated with a large literature review, presented an opportunity to theoretically probe NO_X reduction pathways Ag/Al_2O_3 using NH_3 as a reducing agent. The calculations are based on a reduction path containing intermediate formation of NH_2NO. Reduction of NO is

found to be facile over partially oxidized and hydroxylated Ag via an Eley-Rideal mechanism and a Langmuir-Hinshelwood route is evaluated over oxidized Ag. However, this route involves high barriers which are attributed to formation of stable surface nitrites. These results suggest that nitrite, and subsequently nitrate formation, can poison the oxidized Ag components in the absence of H_2, which is shown to promote hydroxyls (Paper 6) on the Ag surface and consequently could reduce poisoning. Furthermore, reduction of NO_X is considered over hydroxylated Al_2O_3 and shown to occur according to fast-SCR conditions, *i.e.* equal amount of NO and NO_2. The importance of NO_2 is associated with reduced ammonia poisoning of alumina and lower energetics as compared to standard-SCR conditions (only NO). Barriers for NH_2NO decomposition are calculated to be high over Ag. However, via proton exchange reactions with the hydroxylated alumina surface, the barriers are calculated to be substantially lower as compared to the gas-phase isomerization and decomposition of NH_2NO.

Should the scheme in Fig. 4.1 be revised on the basis of this thesis? No, not really, but perhaps the roles of the different components should be modified. Initial reduction of NO (and NO_2) is possible over γ-alumina, but substantially increased in the presence of Ag. However, the alumina support is of equal importance as decomposition of intermediates, such as nitrosamine (NH_2NO) only is found viable over the alumina. This shows that the porous oxide is far from just a support material.

The particular role and importance of small Ag_n clusters is, at this point, highly questionable. In the literature, the existence of such sub-nano Ag phases on Ag/Al_2O_3 is well documented [25, 29, 38, 39] and often discussed in terms of the active phase. The calculations presented in this thesis, however, suggest that silver clusters in the subnano regime have similar chemical properties with respect to SCR reactivity as does metallic and (partially) oxidized silver. Consequently, no particular importance of small Ag_n clusters is found in the context of lean NO_X reduction over Ag/Al_2O_3. However, this does not exclude the possibility that their presence could be vital. Over O- and OH-$p(4\times4)$, the reduction takes place over step Ag atoms (in the Ag_6 subunit), which shows the importance of undercoordinated metal sites. Thus, it is possible that presence of small Ag_n clusters increases the number of such sites, leading to an increased reduction activity. Moreover, as the alumina is shown to be the active component for isomerization and decomposition of intermediates, it is likely that the vicinity of alumina, to the clusters, leads to a higher N_2 yield. Finally, several reports suggests that conversion over high Ag-loading catalysts (>10%) is limited by unselective combustion of the reducing agent [30, 49], correlated to presence of large Ag particles. Thus, it is possible that the presence of silver clusters promotes NO_X reduction selectivity. In order to really understand the role of the Ag_n clusters, more detailed theoretical studies are necessary. First principles calculations are, however, largely dependent on accurate atomistic models because of the size dependent reactivity of Ag_n clusters that have

clear odd-even alternations in *e.g.* adsorption energies. Consequently, calculations of combined Ag_n/Al_2O_3 systems will have to rely on further experimental effort and input regarding the structure and size of these sub-nano clusters.

In a broader context, the presence of partially oxidized silver is shown to increase the activation of the reducing agent. Based on literature data, where the light off temperature for ammonia [50, 57, 59], longchain- [29, 44, 230, 231], and oxygenated hydrocarbons [19–21], is reported around 200 °C, the catalytic reduction activity could be determined by direct access of active sites, *i.e.* partially oxidized Ag. The role of H_2 could be connected to formation of such an Ag charge state. It is known that H_2 lowers the thermal decomposition temperature of silver oxide (Ag_2O) from 330 °C, measured in N_2, to 10°C in pure H_2 [232]. Moreover, when shorter hydrocarbons are used, *e.g.* propene or even methane, the RDS is the partial oxidation and activation of the reducing agent, even in excess of active sites. In this case, the reduction often takes place at high temperatures [44, 230], where unfortunately also direct unselective combustion of the hydrocarbons takes place.

One possibility to increase the low temperature activity, even in the presence of shorter hydrocarbons, could be by doping of Ag/Al_2O_3 with a more potent oxidation metal, *e.g.* platinum. This is currently being done at the Competence Centre for Catalysis and so far with the desired effects [53]. However, with Pt (and other oxidation metals) it is possible that more unselective oxidation takes place; perhaps the very reason why NO_X-SCR over alumina, doped with Ag, shows best results. Furthermore, despite low barriers for NH_3/HC activation and access to important sites, the catalyst surface could be poisoned by the reducing agent; limiting the reduction rate. In order to further improve the Ag/Al_2O_3 catalyst, it would, consequently, be desirable to reduce the poisoning. How to do this is, however, an open issue at this moment.

At this point we have calculated one theoretically viable route for lean NO and NO_2 reduction over Ag/Al_2O_3 with NH_3. This includes the formation and decomposition of NH_2NO and possible effects of H_2. The most natural next step would be to expand this this reaction scheme by including other molecules and intermediates such as NO_3 and NH_4NO_2, among others, and consequently predicting the reaction landscape, based on solely calculations. However, this would essentially lead to a trial- and error approach, which we are trying to avoid in the first place. Perhaps a more suitable next project is to consider the reaction kinetics via a microkinetic model. Such a model would be able to translate the calculated adsorption energies and transition barriers into reaction rates. These rates could then be correlated to experimental data and possibly give further support to the DFT results and provide guidance for future calculations. For example, the calculated barriers for NH_2NO decomposition over Al_2O_3 are low, but because the reaction is calculated to be concerted with four simultaneous proton transfer reactions, it is reasonable to analyze the probability of that reaction. Access to the pre-exponential factors would be of great help. If the factors are calculated to be low, it

is possible that the decomposition reaction is slow and possibly even rate-determining.

Another possibility to address this particular problem, involving NH_2NO decomposition, is via Molecular Dynamics simulations. Constraining one of the four proton reaction coordinates and changing it stepwise for each dynamics simulation will clarify if the concerted reaction occurs as a domino effect, *i.e.* as soon as one proton transfer occurs it drives the reaction of the consecutive ones.

Because this particular catalytic system is difficult to approach from both an experimental and theoretical point of view much of the current scientific activities are still based on a trial- and error approach. However, there are projects at the Competence Centre for Catalysis, among others, where chemical engineering and surface science experiments are combined with theoretical approaches in order to understand catalytic processes and characterize catalyst materials on a fundamental level. This thesis is part of one such project where the combination of experiments and theory was fundamental in order to reduce the complexity of the Ag/Al_2O_3 system and enable direct comparison between measurements and calculations. After all, the pressure and materials gaps are still largely present and, consequently, the notion of catalyst design is still confined to well defined catalysts materials and conditions that can be probed experimentally and theoretically with comparable atomic resolution. Experiments and theory are thus strongly correlated. Experimental spectroscopy measurements based on *e.g* XPS and IR, are often difficult to interpret and assignments to measured signatures are often based on tradition and literature. With theoretical first principles calculations these signatures can, however, be separated and assigned to individual species. In return, the complexity of a catalytic system, such as NO_X reduction over Ag/Al_2O_3, is a clear limiting factor for atomistic calculations where input from experimental measurements plays a key role. Today, calculations with up to $\sim$1000 atoms are possible with quantum mechanical description depending on xc-functionals, pseudopotentials, basis-sets, and sometimes even the practical numerical implementation and the computer architecture (software and hardware). However, what is critical for theoretical first principles calculations is access to accurate atomistic models. These models are largely derived from experimental characterization measurements. To some extent, DFT can be used to probe the potential energy surface and calculate the low energy atomic structures, but this is limited to clusters and simple surface structures. For large, multicomponent systems, such as Ag/Al_2O_3 this is not realistic.

Density functional theory calculation have numerous times proven to be highly valuable for characterizing, probing, verifying, and understanding chemical structures, properties, and reactions at the atomic scale. DFT can be used to understand and even predict experiments, but also to derive trends and draw qualitative conclusions regarding the reactivity of molecules and solid materials as changes in composition and structure are induced. However, density functional theory can also be used to study

a specific questions and address a problem that cannot be approached experimentally. This thesis contains several such studies, for example: the reversed core level shifts of oxidized Ag, the structure and reactivity of small Ag_n clusters, sites on Ag/Al_2O_3 for dissociation of H_2, adsorption of NH_3 and NO_X, and the role of Ag and Ag_n for the lean NO_X-SCR activity.

Acknowledgements

The work was performed at the Competence Centre for Catalysis which is hosted by Chalmers University of Technology and financially supported by the Swedish Energy Agency and the member companies: AB Volvo, Volvo Car Corporation AB, ECAPS AB, Haldor Topsøe A/S, and Scania CV AB.

The Swedish Research Council (VR), SSF (FUNCAT-project), Nordforsk, and The Royal Society of Arts and Sciences in Gothenburg (KVVS) are gratefully acknowledged for the financial support.

Calculations have been performed at C3SE (Göteborg) and PDC (Stockholm).

Henrik Grönbeck Jag känner mig obeskrivligt priviligerad som fått ha dig som huvudhandledare under dessa år. Oerhört stort tack för att du delat med dig av din kunskap och alltid varit tillgänglig för diskussioner och handledning. Det stöd, engagemang och entusiasm som jag upplevt varje dag under min doktorandtid värderar jag enormt. Tack för allt.

Anders Hellman Det sägs att bara den som kan och förstår ett komplicerat ämne i detalj är kapabel att förklara ämnet på ett enkelt sätt. Du förklarar allt på ett enkelt sätt. Vad säger det om din kunskap? Det har varit ett sant nöje och en stor förmån att få insikt i din kunskap och tack för all hjälp, goda råd och stöd.

Magnus Skoglundh I am grateful for the chance to perform my graduate studies at KCK, and even more so for all the comments and advice.

Itai Panas For all the discussions, and suggestions.

Göran Wahnström Thank you for all the guidance and help.

I had the opportunity to visit **Bjørk Hammer** and his group (**Henrik**, **Jakob**, **Katrine**, **Mie**, **Lasse**, **Umberto**, **Anton**, and **Lara**) in Århus. I am very grateful to Bjørk for the opportunity, the disscussions and the hospitality that I recieved during my stay.

I have had several fruitful collaborationsi during these years. This includes **Andreas Sternig** and **Oliver Diwald** in Erlangen, and many collaborations in Lund. I am particularly gratelful to **Natalia M. Martin** and **Edvin Lundgren** for introducing me to XPS and, more importantly, for all the collaborations and discussions.

The computational team at KCK: **Adriana**, **Jakub**, **Maxime**, **Dr. Paz-Borbon** (I will never here the end of it otherwise), and **Samira** for the atmosphere and discussions about everything and anything.

Hanna Härelind For being patient, supportive and always happy.

Fredrik, **Hannes**, and **Soran** for all the good times, laughs, and foods consumed.

All the collegues and friends at KCK, Chemical Physics, and Applied Surface Chemistry. In particular: **Sheedeh**, **Djamela**, **Hanna G.**, **Marika**, **Emma A.**, **Linda**, **Alexander S.**, **Pooya**, **Björn W.**, and **Stephanie** for all the discussions lately.

During the last months a few frienships have been neglected that I will try to make up, most importantly **Jonatan** and **Robin**.

Det finns vissa som bidragit i det tysta men alltid varit stöttande och närvarande och jag är evigt tacksam och glad för ha dem: mamma (**Mubera**), moster (**Fatima**) och syster (**Sena**).

Adriana Den som har stöttat mest, haft oändlig med tålamod och förståelse och alltid ställt upp i jobb och vardag. Det finns inget tack stort nog till dig.

Bibliography

[1] Erisman, J. W., Sutton, M. A., Galloway, J., Klimont, Z., and Winiwarter, W. (2008) *Nature Geoscience* **1**, 636.

[2] Tamaru, K. (1991) The history of the development of ammonia synthesis In J. R. Jennings, (ed.), Catalytic Ammonia Synthesis: Fundamentals and Practice, chapter 1, pp. 1–17 Plenum Press, New York.

[3] Dahl, S., Logadottir, A., Egeberg, R. C., Larsen, J. H., Chorkendorff, I., Törnqvist, E., and Nørskov, J. K. (2012) *App. Catal. B* **113**, 228.

[4] Lauritsen, J. V., Nyberg, M., Nørskov, J. K., Clausen, B. S., Topsøe, H., Lægsgaard, E., and Besenbacher, F. (2004) *J. Catal.* **224**, 94.

[5] Hellman, A., Resta, A., Martin, N. M., Gustafson, J., Trinchero, A., Carlsson, P.-A., Balmes, O., Felici, R., van Rijn, R., Frenken, J. W. M., Andersen, J. N., Lundgren, E., and Grönbeck, H. (2012) *J. Phys. Chem. Lett.* **3**, 678.

[6] http://www.epa.gov/airquality/carbonmonoxide/ (07-08-11).

[7] Chorkendorff, I. and Niemantsverdriet, W. (2007) Concepts of Modern Catalysis and Kinetics, Wiley-VCH, Weinheim, 2nd edition.

[8] Burch, R. (2005) *Catal. Rev.* **46**, 271.

[9] Li, Y. and Armor, J. N. (1992) *Appl. Catal. B* **1**, L31.

[10] Yogoa, K., Ihara, M., Terasaki, I., and Kikuchi, E. (1993) *Appl. Catal. B* **2**, L1.

[11] Parvulescu, V. I., Grange, P., and Delmon, B. (1998) *Catal. Today* **46**, 233.

[12] Kintaichi, Y., Hamada, H., Tabata, M., Sasaki, T. Y. M., and Ito, T. (1990) *Catal. Lett.* **6**, 239.

[13] Hamada, H., Kintaichi, Y., Sasaki, M., and Ito, T. (1991) *Appl. Catal. B* **75**, L1.

[14] Hamada, H., Kintaichi, Y., Inaba, M., Tabata, M., Yoshinari, T., and Tsuchida, H. (1996) *Catal. Today* **29**, 53.

[15] Radtke, F., Koeppel, R. A., Minardi, E. G., and Baiker, A. (1997) *J. Catal.* **167**, 127.

[16] Obuchi, A., Ohi, A., Nakamura, M., Ogata, A., Mizuno, K., and Ohuchi, H. (1993) *Appl. Catal. B* **2**, 71.

[17] Burch, R. and Watling, T. C. (1997) *Catal. Lett.* **43**, 19.

[18] Burch, R., Fornasiero, P., and Watling, T. C. (1998) *J. Catal.* **176**, 204.

[19] Miyadera, T. and Yoshida, K. (1993) *Chem. Lett.* **2**, 1483.

[20] Miyadera, T. (1993) *Appl. Catal. B* **2**, 199.

[21] Miyadera, T. (1997) *Appl. Catal. B* **13**, 159.

[22] Kung, M. C., Bethke, K. A., Yan, J., Lee, J. H., and Kung, H. H. (1997) *Appl. Surf. Sci.* **121-122**, 261.

[23] Haneda, M., Kintaichi, Y., Inaba, M., and Hamada, H. (1997) *Appl. Surf. Sci.* **121-122**, 391.

[24] Hoost, T. E., Kudla, R. J., Collins, K. M., and Chattha, M. S. (1997) *Appl. Catal. B* **13**, 59.

[25] Bethke, K. A. and Kung, H. H. (1997) *J. Catal.* **172**, 93.

[26] Meunier, F. C., Breen, J. P., Zuzaniuk, V., Olsson, M., and Ross, J. R. H. (1999) *J. Catal.* **187**, 493.

[27] Wang, J., Aguilar-Rios, G., and Wang, R. (1999) *Appl. Surf. Sci.* **147**, 44.

[28] Satokawa, S. (2000) *Chem. Lett.* **29**, 294.

[29] Shimizu, K., Shibata, J., Yoshida, H., Satsuma, A., and Hattori, T. (2001) *Appl. Catal. B* **30**, 151.

[30] Burch, R., Breen, J. P., and Meunier, F. C. (2002) *Appl. Catal. B* **39**, 283.

[31] Bogdanchikova, N., Meunier, F., Avalos-Borja, M., Breen, J. P., and Pestryakov, A. (2002) *Appl. Catal. B* **36**, 287.

[32] Iglesias-Juez, A., Hungria, A. B., Martinez-Arias, A., Fuerte, A., Fernandez-Garcia, M., Anderson, J. A., Conesa, J. C., and Soria, J. (2003) *Appl. Catal. B* **36**, 287.

[33] Satokawa, S., Shibata, J., Shimizu, K., Satsuma, A., and Hattori, T. (2003) *Appl. Catal.* **42**, 179.

[34] Bion, N., Saussey, J., Haneda, M., and Daturi, M. (2003) *J. Catal.* **217**, 47.

[35] Shibata, J., Takada, Y., Shichi, A., Satokawa, S., Satsuma, A., and Hattori, T. (2004) *J. Catal.* **222**, 368.

[36] Richter, M., Bentrup, U., Eckelt, R., Schneider, M., Pohl, M. M., and Fricke, R. (2004) *Appl. Catal. B* **51**, 261.

[37] He, H. and Yu, Y. (2005) *Catal. Tod.* **100**, 37.

[38] Breen, J. P., Burch, R., Hardacre, C., and Hill, C. J. (2005) *J. Phys. Chem. B* **109**, 4805.

[39] Sazama, P., Capek, L., Drobna, H., Sobalik, Z., Dedecek, J., Arve, K., and Wichterlova, B. (2005) *J. Catal.* **232**, 302.

[40] Wichterlová, B., Sazama, P., Breen, P., Burch, R., Hill, C. J., Čapek, L., and Sobalík, Z. (2002) *J. Catal.* **235**, 195.

[41] Shimizu, K. and Satsuma, A. (2006) *Phys. Chem. Chem. Phys.* **8**, 2677.

[42] Zhang, X., He, H., Gao, H., and Yu, Y. (2008) *Spectrochemica Acta Part A* **71**, 1445.

[43] He, H., Zhang, X., Wy, Q., Zhang, C., and Yu, Y. (2008) *Catal. Surf. Asia* **12**, 38.

[44] Kannisto, H., Härelind Ingelsten, H., and Skoglundh, M. (2009) *J. Mol. Catal. A* **302**, 86.

[45] Tham, Y. F., Chen, J.-Y., and Dibble, R. W. (2008) *Proc. Comb. Inst.* **32**, 2827.

[46] Stakheev, A. Y., Pributkov, P. V., Dahl, S., Baeva, G. N., Bragina, G. O., and Telegina, N. S. (2009) *Top. Catal.* **52**, 1821.

[47] Sawabe, K., Hiro, T., Shimizu, K., and Satsuma, A. (2010) *Catal. Tod.* **153**, 90.

[48] Korhonen, S. T., Beale, A. M., Newton, M. A., and Weckhuysen, B. M. (2011) *J. Chem. Phys. C* **115**, 885.

[49] Shimizu, K., Sawabe, K., , and Satsuma, A. (2011) *Catal. Sci. Technol.* **1**, 331.

[50] Doronkin, D., Fogel, S., Tamm, S., Olsson, L., Khan, T. S., Bligaard, T., Gabrielsson, P., and Dahl, S. (2012) *App. Catal. B* **113-114**, 228.

[51] Kannisto, H., Arve, K., Pingel, T., Hellman, A., Härelind, H., Eränen, K., Olsson, E., Skoglundh, M., and Murzin, D. Y. (2013) *Catal. Sci. Technol.* **3**, 644.

[52] Hellman, A. and Grönbeck, H. (2008) *Phys. Rev. Lett.* **100**, 116801.

[53] Gunnarsson F., Kannisto H., Skoglundh M., and Härelind H. *In preparation.*

[54] Morterra, C. and Magnacca, G. (1996) *Catal. Today* **27**, 497.

[55] Wischert, R., Laurent, P., Copret, C., Delbecq, F., and Sautet, P. (2012) *J. Amer. Chem. Soc.* **134**, 14430.

[56] DeCanio, E. C., Edwards, J. C., and Bruno, J. W. (1994) *J. Catal.* **148**, 76.

[57] Gang, L., Anderson, B. G., vanGrondelle, J., and vanSanten, R. A. (2003) *App. Catal. B* **40**, 101.

[58] Richter, M., Fricke, R., and Eckelt, R. (2004) *Catal. Lett.* **94**, 115.

[59] Kondratenko, E. V., Kondratenko, V. A., Richter, M., and Fricke, R. (2006) *J. Catal.* **239**, 23.

[60] Shimizu, K. I. and Satsuma, A. (2007) *Appl. Catal. B* **77**, 202.

[61] Obuchi, A., Wögerbauer, C., Köppel, R., and Baiker, A. (1998) *Appl. Catal. A* **19**, 9.

[62] Tamm, S., Ingelsten, H. H., and Palmqvist, A. (2008) *J. Catal.* **255**, 304.

[63] Amiridis, M. D., Zhang, T. J., and Farrauto, R. J. (1996) *Appl. Catal, B* **10**, 203.

[64] Fritz, A. and Pitchon, V. (1997) *Appl. Catal B* **13**, 1.

[65] Hohenberg, P. and Kohn, W. (1964) *Phys. Rev.* **136**, 864.

[66] Kohn, W. and Sham, L. J. (1965) *Phys. Rev.* **140**, A1133.

[67] Jones, R. O. and Gunnarsson, O. (1989) *Rev. Mod. Phys.* **61**, 689.

[68] Kohn, W., Becke, A. D., and Parr, R. (1996) *J. Phys. Chem.* **100**, 12974.

[69] Martin, R. M. (2004) Electronic Structure: Basic Theory and Practical Methods, Cambridge University Press, Cambridge, reprinted edition.

[70] Kohanoff, J. (2006) Electronic Structure Calculations for Solids and Molecules: Theory and Computational Methods, Cambridge University Press, Cambridge, 1st edition.

[71] Born, M. and Oppenheimer, R. (1927) *Ann. Physik* **87**, 457.

[72] Hartree, D. R. (1927) *Proc. Cambridge Phil. Soc.* **24**, 111.

[73] Hartree, D. R. (1927) *Proc. Cambridge Phil. Soc.* **24**, 310.

[74] Hartree, D. R. (1927) *Proc. Cambridge Phil. Soc.* **24**, 426.

[75] Slater, J. C. (1928) *Phys. Rev.* **32**, 339.

[76] Fock, V. (1930) *Z. Phys.* **61**, 126.

[77] Thomas, L. H. (1927) *Proc. Cambridge Phil. Soc.* **26**, 376.

[78] Fermi, E. (1927) *Rend. Accad. Naz. Lincei* **6**, 602.

[79] Perdew, J., Chevary, J. A., Vosko, S. H., Jackson, K. A., Pederson, M. R., Singh, D. J., and Fiolhais, C. (1992) *Phys. Rev. B* **46**, 6671.

[80] Perdew, J., Burke, K., and Ernzerhof, M. (1996) *Phys. Rev. Lett.* **77**, 3865.

[81] Zhang, Y. and Yang, W. (1998) *Phys. Rev. Lett.* **80**, 890.

[82] Hammer, B., Hansen, L. B., and Nørskov, J. K. (1999) *Phys. Rev. B* **59**, 7413.

[83] Hammer, B., Jacobsen, K. W., and Nørskov, J. K. (1993) *Phys. Rev. Lett.* **70**, 3971.

[84] Kurth, S., Perdew, J. P., and Blaha, P. (1999) *Int. J. Quant. Chem.* **75**, 889.

[85] Adamo, C. and Barone, V. (1999) *J. Chem. Phys.* **110**, 6158.

[86] Becke, A. D. (1993) *J. Phys. Chem.* **98**, 5648.

[87] Martins, J. L., Buttet, J., and Car, R. (1985) *Phys. Rev. B* **31**, 1804.

[88] Examples of LCAO programs that utilize Gaussian orbitals are: Gaussian, TURBOMOLE, and PSI.

[89] Examples of LCAO programs that utilize Slater orbitals are: ADF, and CASINO.

[90] Examples of LCAO programs that utilize numerical orbitals are: Dmol and SIESTA.

[91] Car, R. and Parrinello, M. (1985) *Phys. Rev. Lett.* **55**, 22.

[92] Hamann, D. R., Schlüter, M., and Chiang, C. (1979) *Phys. Rev. Lett* **43**, 1494.

[93] Troullier, N. and Martins, J. L. (1992) *Phys. Rev. B* **46**, 1754.

[94] Vanderbilt, D. (1990) *Phys. Rev. B* **41**, 7892.

[95] Grönbeck, H. (2004) *Top. Catal.* **28**, 59.

[96] We have used DMol, version 4.0.

[97] All calculations are performed with a gradient corrected PBE functional. In a LCAO implementation, the KS one-electron orbitals where expanded in a local nummerical basis set (dnp). Moreover, bottom two layers where held fixed at all time, in order to simulate bulk material. The surfaces where cut from the optimized bulk. The calculated (experimental) lattice parameters for Mg in a hexagonal unit cell are: a=b=3.18, c=5.16 (a=b=3.21, c=5.21) Å . The corresponding value for MgO is 4.26 (4.21) Å.

[98] Monkhorst, H. J. and Pack, J. D. (1976) *Phys. Rev. B* **13**, 5188.

[99] Pack, J. D. and Monkhorst, H. J. (1977) *Phys. Rev. B* **16**, 1748.

[100] Pulay, P. (1969) *Mol. Phys.* **17**, 197.

[101] Wilson, E. B., Decius, J. C., and Gross, P. C. (1955) Molecular Vibrations, Dover: New York, original edition.

[102] Henkelman, G., Jóhannesson, G., and Jónsson, H. (2002) *Theoretical Methods on Condensed Phase Chemistry* **5**, 269.

[103] Olsen, R. A., Kroes, G. J., Henkelman, G., Arnaldsson, A., and Jónsson, H. (2004) *J. Chem. Phys.* **121**, 9776.

[104] Halgren, T. A. and Lipscomb, W. N. (1977) *Chem. Phys. Lett.* **49**, 225.

[105] Hestenes, M. R. and Stiefel, E. (1952) *J. Res. Nat. Bur. Stand.* **46**, 409.

[106] Reuter, K. and Scheffler, M. (2002) *Phys. Rev. B* **65**, 035406.

[107] Rogal, J. and Reuter, K. (2007) *Educational Notes RTO-EN-AVT-142, Neuilly-sur-Seine* pp. 2–1.

[108] P.J. Linstrom and W.G. Mallard, Eds., **NIST Chemistry WebBook, NIST Standard Reference Database Number 69**, National Institute of Standards and Technology, Gaithersburg MD, 20899, *http://webbook.nist.gov*, (retrieved February 15, 2010).

[109] Schnadt, J., Michaelides, A., Knudsen, J., Vang, R. T., Reuter, K., Lægsgaard, E., Scheffler, M., and Besenbacher, F. (2006) *Phys. Rev. Lett.* **96**, 146101.

[110] Schmidt, M., Reicho, A., Stierle, A., Costina, I., Klikovits, J., Kostelnik, P., Dubay, O., Kresse, G., Gustafson, J., Lundgren, E., Andersen, J. N., Dosch, H., and Varga, P. (2006) *Phys. Rev. Lett.* **96**, 146102.

[111] G. Binnig, H. R. (1986) *IBM J. Res. Dev.* **30**, 355.

[112] Bardeen, J. (1961) *Phys. Rev. Lett.* **6**, 57.

[113] J. Tersoff, D. R. H. (1983) *Phys. Rev. Lett.* **50**, 1998.

[114] García, S. G., Salinas, D. R., and Staikov, G. (2005) *Surf. Sci.* **576**, 1.

[115] Reichelt, R., Günter, S., Rößler, M., Wintterlin, J., Kubias, B., Jakobi, B., and Schlög, R. (2007) *Phys. Chem. Chem. Phys.* **9**, 3590.

[116] Chen, C. J. (1990) *Phys. Rev. Lett.* **60**, 448.

[117] Chen, C. J. (1991) *Phys. Rev. B* **42**, 8841.

[118] W. A Hofer, A. S. Foster, A. L. S. (2003) *Rev. Mod. Phys.* **75**, 1287.

[119] J. M. Blanco, F. Flores, R. P. (2006) *Prog. Surf. Sci.* **81**, 403.

[120] Baykara, M. Z., andH. Mönig, M. T., Schwendemann, T. C., Ünverdi, Ö., Rodrigo, L., Altman, E. I., Pérez, R., and Schwarz, U. D. (2013) *Phys. Rev. B* **87**, 155414.

[121] Tsyganenko, A. A. and Filimonov, V. N. (1973) *J. Mol. Struct.* **19**, 579.

[122] Abello, M. C., Velasco, A. P., Gorriz, O. F., and Rivarola, J. B. (1995) *Appl. Catal. A* **129**, 93.

[123] Ealet, B., Wlyakhlouffi, M. H., Gillet, E., and Ricci, M. (1994) *Thin Solid Films* **250**, 92.

[124] Zhang, W., Sun, M., and Prins, R. (2002) *J. Phys. Chem.* **106**, 11805.

[125] Klingstedt, F., Arve, K., Eränen, K., and Murzin, D. Y. (2006) *Acc. Chem. Res.* **39**, 273.

[126] Koebel, M., Madia, G., and Elsener, M. (2002) *Catal. Today* **73**, 239.

[127] Nova, I., Ciardelli, C., Tronconi, E., Chatterjee, D., and Bandl-Konrad, B. (2006) *Catal. Today* **114**, 3.

[128] Nova, I., Ciardelli, C., Tronconi, E., Chatterjee, D., and Weibel, M. (2007) *Top. Catal.* **42**, 43.

[129] Sjövall, H., Fridell, E., Blint, R. J., and Olsson, L. (2007) *Top. Catal.* **42**, 113.

[130] Grossale, A., Nova, I., Tronconi, E., Chatterjee, D., and Weibel, M. (2009) *Top. Catal.* **52**, 13.

[131] Sjövall, H., Blint, R. J., and Olsson, L. (2009) *App. Catal. B* **92**, 138.

[132] Sjövall, H., Blint, R. J., and Olsson, L. (2009) *J. Phys. Chem C* **113**, 1393.

[133] Yin, X., Han, H., and Miyamoto, A. (2000) *Phys. Chem. Chem. Phys.* **2**, 4243.

[134] Anstrom, M., Dumesic, J. A., and Topsøe, N.-Y. (2002) *Catal. Lett.* **78**, 1.

[135] Anstrom, M., Topsøe, N.-Y., and Dumesic, J. A. (2003) *J. Catal.* **213**, 115.

[136] Soyer, S., Uzun, A., Senkan, S., and Onal, I. (2006) *Catal. Today* **118**, 268.

[137] Li, J. and Li, S. (2007) *Phys. Chem. Chem. Phys.* **9**, 3304.

[138] Li, J. and Li, S. (2008) *J. Phys. Chem. C* **112**, 16938.

[139] Gao, X., Du, X., Jiang, Y., Lou, Z., and Cen, K. (2010) *J. Mol. Catal. A* **317**, 46.

[140] Gruber, M. and Hermann, K. (2013) *J. Chem. Phys.* **138**, 094704.

[141] Eränen, K., Lindfors, L.-E., Klingstedt, F., and Murzin, D. Y. (2003) *J. Catal.* **219**, 25.

[142] Brosius, R., Arve, K., Groothaert, M. H., and Martens, J. A. (2005) *J. Catal.* **231**, 344.

[143] Seriani, N. and Mittendorf, F. (2008) *J. Phys. Condens. Matter* **20**, 184023.

[144] Hammond, J. S., Gaarenstroom, S. W., and Winograd, N. (1975) *Anal. Chem.* **47**, 2193.

[145] Campbell, C. T. (1985) *Surf. Sci.* **157**, 43.

[146] van Santen, R. A. and Kuipers, H. P. C. E. (1987) *Adv. Catal.* **35**, 265.

[147] Carter, E. A. and Goddard, W. A. (1989) *Surf. Sci.* **209**, 243.

[148] Besenbacher, F. and Nørskov, J. (1993) *Progress in Surf. Sci.* **44**, 5.

[149] Bukhtiyarov, V. I., Kondratenko, V. A., and Boronin, A. I. (1993) *Surf. Sci. Lett.* **293**, L826.

[150] Nakatsuji, H. and Nakai, H. (1993) *J. Chem. Phys.* **98**, 2433.

[151] Andersen, J. N., Hennig, D., Lundgren, E., Methfessel, M., Nyholm, R., and Scheffler, M. (1994) *Phys. Rev. B* **50**, 17525.

[152] Wang, L. and Billing, G. D. (1997) *Chem. Phys.* **224**, 65.

[153] Linic, S. and Barteau, M. A. (2002) *J. Am. Chem. Soc* **124**, 310.

[154] Reuter, K., Ganduglia-Pirovano, M. V., Stampfl, C., and Scheffler, M. (2002) *Phys. Rev. B* **65**, 165403.

[155] Linic, S. and Barteau, M. A. (2003) *J. Am. Chem. Soc* **125**, 4034.

[156] Linic, S. and Barteau, M. A. (2003) *J. Catal.* **214**, 200.

[157] Li, W., Stampfl, C., and Scheffler, M. (2003) *Phys. Rev. B* **67**, 045408.

[158] Li, W., Stampfl, C., and Scheffler, M. (2003) *Phys. Rev. B* **68**, 165412.

[159] Michaelides, A., Bocquet, M. L., Sautet, P., Alavi, A., and King, D. A. (2003) *Chem. Phys. Lett.* **367**, 344.

[160] Bukhtiyarov, V. I., Havecker, M., Kaichev, V. V., Knop-Gericke, A., Mayer, R., and Schlög, R. (2003) *Phys. Rev. B* **67**, 235422.

[161] Lundgren, E., Gustafson, J., Mikkelsen, A., Andersen, J. N., Stierle, A., Dosch, H., Todorova, M., Rogal, J., Reuter, K., and Scheffler, M. (2004) *Phys. Rev. Lett.* **92**, 046101.

[162] Stegelmann, C., Schiodt, N. C., Campbell, C. T., and Stoltze, P. (2004) *J. Catal.* **221**, 630.

[163] Xu, Y., Greeley, J., and Mavrikakis, M. (2005) *J. Am. Chem. Soc.* **127**, 12823.

[164] Michaelides, A., Reuter, K., and Scheffler, M. (2005) *J. Vac. Sci. Technol. A* **23**, 1487.

[165] Mohammad, A. B., Lim, K. H., Yudanov, I. V., Neyman, K. M., and R"osch, N. (2007) *Phys. Chem. Chem. Phys.* **9**, 1247.

[166] Seriani, N. and Mittendorfer, F. (2008) *J. Phys.: Condens. Matter* **20**, 184023.

[167] Schnadt, J., Knudsen, J., Hu, X. L., Michaelides, A., Vang, R. T., Reuter, K., Li, Z. S., Lægsgaard, E., Scheffler, M., and Besenbacher, F. (2009) *Phys. Rev. B* **80**, 075424.

[168] Rovida, G., Pratesi, F., Maglietta, M., and Ferroni, E. (1972) *J. Vac. Sci Technol.* **9**, 796.

[169] Carlisle, C. I., Fujimoto, T., Sim, W. S., and King, D. A. (2000) *Surf. Sci.* **470**, 15.

[170] Siegbahn, K. (1982) *Rev. Mod Phys.* **54**, 709.

[171] Gaarenstroom, S. W. and Winograd, N. (1977) *J. Chem. Phys.* **67**, 3500.

[172] Kaaushik, V. K. (1991) *J. Electron Spectrosc. Relat. Phenom.* **56**, 273.

[173] Tjeng, L. H., Meinders, M. B. J., van Elp, J., J.Ghijsen, Sawatzky, G. A., and Johnson, R. L. (1990) *Phys. Rev. B* **41**, 3190.

[174] Henkelman, G., Arnaldsson, A., and Jónsson, H. (2006) *Comput. Mater. Sci.* **36**, 354.

[175] Lindberg, B., Hamrin, K., Johansson, G., Gelius, U., Fahlman, A., Nordling, C., and Siegbahn, K. (1970) *Phys. Scr.* **1**, 286.

[176] Weinert, M. and Watson, R. E. (1995) *Phys. Rev. B* **51**, 17168.

[177] Abrikosov, I. A., Olovsson, W., and Johansson, B. (2001) *Phys. Rev. Lett.* **87**, 176403.

[178] Newns, D. M. (1969) *Phys. Rev.* **178**, 1123.

[179] Mavrikakis, M., Hammer, B., and Nørskov, J. K. (1998) *Phys. Rev. Lett.* **81**, 2819.

[180] Hammer, B. and Nørskov, J. K. (2002) *Nature* **376**, 238.

[181] Nilsson, A., Pettersson, L. G. M., Hammer, B., Bligaard, T., Christensen, C. H., and Nørskov, J. K. (2005) *Catal. Lett.* **100**, 111.

[182] Ertl, G. (1994) *Surf. Sci.* **299**, 742.

[183] Hammer, B. (2006) *Top. Catal.* **37**, 3.

[184] Honkala, K., Hellman, A., Remediakis, I. N., Logadottir, A., Carlsson, A., Dahl, S., Christensen, C. H., and Nørskov, J. K. (2005) *Science* **307**, 555.

[185] Sato, K., Yoshinari, T., Kintaichi, Y., Haneda, M., and Hamada, H. (2003) *Appl. Catal. B* **44**, 67.

[186] Sato, K., Yoshinari, T., Kintaichi, Y., Haneda, M., and Hamada, H. (2003) *Catal. Commun.* **4**, 315.

[187] Satsuma, A., Shibata, J., Shimizu, K., and Hattori, T. (2005) *Catal. Surv. Asia* **9**, 75.

[188] Rey, C., Gallego, L. J., Garciarodeja, J., Alonso, J. A., and Iniguez, M. P. (1993) *Phys. Rev. B* **48**, 8253.

[189] Michaelian, K. and Garzon, N. R. I. L. (1999) *Phys. Rev. B* **60**, 2000.

[190] Fernandez, E. M., Soler, J. M., Garzon, I. L., and Balbas, L. C. (2004) *Phys. Rev. Lett.* **70**, 165403.

[191] Alameddin, G., Hunter, J., Cameron, D., and Kappes, M. M. (1992) *Chem. Phys. Lett.* **192**, 122.

[192] Lian, L., Hackett, P. A., and Rayner, D. M. (1993) *J. Chem. Phys.* **99**, 2583.

[193] Avdeev, V. I., Ruzankin, S. F., and Zhidomirov, G. M. (1997) *J. Stru. Chem.* **38**, 519.

[194] Bonacic-Koutecky, V., Boiron, M., Pittner, J., Fantucci, P., and Koutecky, J. (1999) *Euro. Phys. J.* **9**, 183.

[195] Fournier, R. (2001) *J. Chem. Phys.* **115**, 2165.

[196] Hagen, J. et al. (2004) *J. Amer. Chem. Soc.* **26**, 3442.

[197] Socaciu, L. D., Hagen, J., Roux., J. L., Popolan, D. M., Bernhardt, T. M., and Wöste, L. (2004) *J. Chem. Phys.* **120**, 2078.

[198] Berhardt, T. M. (2005) *Int. J. Mass Spect.* **243**, 1.

[199] Bernhardt, T. M., Socaciu-Siebert, L. D., Hagen, J., and Wöste, L. (2005) *App. Cat. A* **291**, 170.

[200] Zhou, J., Li, Z.-H., Wang, W.-N., and Fan, K.-N. (2006) *J. Phys. Chem. A* **7167**, 7167.

[201] Bürgel, C., Mitric, R., and Bonacic-Koutecky, V. (2006) *Appl. Phys. A* **82**, 117.

[202] Geusic, M. E., Morsé, M. D., and Smalley, R. E. (1985) *J. Chem. Phys.* **82**, 590.

[203] Jackschath, C., Rabin, I., and Schulze, W. (1992) *Z. Phys. D* **22**, 517.

[204] Taylor, K. J., Pettiette-Hall, C. L., Cheshnovsky, O., and Smalley, R. E. (1992) *J. Chem. Phys.* **96**, 3319.

[205] Billas, I. M. L., Châtelain, A., and de Heer, W. A. (1994) *Science* **265**, 1682.

[206] Whetten, R. L., Cox, D. M., Trevor, D. J., and Kaldor, A. (1985) *Phys. Rev. Lett.* **54**, 1494.

[207] Panas, I., Schule, J., Siegbahn, P., and Wahlngren, U. (1988) *Chem. Phys. Lett.* **1149**, 265.

[208] de Heer, W. A. (1993) *Rev. Mod. Phys.* **65**, 611.

[209] Brack, M. (1993) *Rev. of Mod. Phys.* **65**, 677.

[210] Fedrigo, E., Harbish, W., Belyaev, J., and Buttet, J. (1993) *Chem. Phys. Lett.* **211**, 166.

[211] Grönbeck, H. and Rosen, A. (1996) *Z. Phys. D* **36**, 153.

[212] Alonso, J. A. (2000) *Chem. Rev.* **100**, 637.

[213] Lide, D. R. (1990-1991) Handbook of Chemistry and Physics, CRC Press, Inc., 71 edition.

[214] Molina, L. M. and Hammer, B. (2003) *Phys. Rev. Lett.* **90**, 206102.

[215] Molina, L. M., Rasmussen, M. D., and Hammer, B. (2004) *J. Chem Phys.* **120**, 7673.

[216] Broqvist, P., Molina, L. M., Grönbeck, H., and Hammer, B. (2004) *J. Catal.* **227**, 217.

[217] Hammer, B. (2002) *Phys. Rev. Lett.* **89**, 016102.

[218] Knözinger, H. and Ratnasamy, P. (1978) *Catal. Rev.-Sci. Eng.* **17**, 31.

[219] Fleicher, M. B., Golender, L. O., and Shimanskaya, M. V. (1991) *J. Chem. Soc. Faraday Trans.* **87**, 745.

[220] Fernández-Sanz, J., Rabaâ, H., Poveda, F. M., Máeques, A., and Calzado, C. J. (1998) *Int. J. Quantum Chem.* **70**, 359.

[221] Sohlberg, K., Pennycook, S. J., and Pantelides, S. T. (1999) *J. Am. Chem. Soc.* **121**, 10999.

[222] Ionescu, A., Allouche, A., Aycard, J. P., Rajzmann, M., and Hutschka, F. (2002) *J. Phys. Chem. B* **106**, 9359.

[223] Digne, M., Sautet, P., Raybaud, P., Euzen, P., and Toulhoat, H. (2002) *J. Catal.* **211**, 1.

[224] Digne, M., Sautet, P., Raybaud, P., Euzen, P., and Toulhoat, H. (2004) *J. Catal.* **226**, 54.

[225] Liu, Z., Ma, L., and Junaid, A. S. M. (2010) *J. Phys. Chem. C* **114**, 4445.

[226] Holmgren, L., Grönbeck, H., Andersson, M., and Rosen, A. (1996) *Phys. Rev. B* **53**, 16644.

[227] HOMO: Highest occupied molecular orbital. LUMO: Lowest unoccupied molecular orbital.

[228] Zorn, K., Giorgio, S., Halwax, E., Henry, C. R., Grönbeck, H., and Rupprechter, G. (2011) *J. Phys. Chem.* **115**, 1103.

[229] All calculations are performed with a gradient corrected PBE functional. In a LCAO implementation, the KS one-electron orbitals where expanded in a local nummerical basis set (dnp). CO in the gas phase is calculated with a bond length of 1.14 Å, a binding energy of 11.32 eV , and a vibrational frequency of 2117 cm^{-1}. The corresponding experimental values are 1.13 Å, 11.09 eV, and 2170 cm^{-1}.

[230] Shimizu, K., Satsuma, A., and Hattori, T. (2000) *Appl. Catal. B* **25**, 239.

[231] Lindfors, L.-E., Eränen, K., Klingstedt, F., and Murzin, D. Y. (2004) *Top. Catal.* **28**, 185.

[232] Nakamori, I., Nakamura, H., Hayano, T., and Kagawa, S. (1974) *Bull. Chem. Soc. Japan* **47**, 1827.